AN OPTIMIZED ANISOTROPIC PRESSURE FLUCTUATION MODEL FOR THE SIMULATION OF TURBULENCE-INDUCED VIBRATIONS

K. Zwijsen[a,*], A. Marreiros de Freitas[b,c], S. Tajfirooz[a], E.M.A. Frederix[a], A.H. van Zuijlen[d]

[a]Nuclear Research and consultancy Group (NRG), Westerduinweg 3, 1755 LE Petten, The Netherlands
[b]Department of Physics and INFN, University of Rome "Tor Vergata", Via della Ricerca Scientifica 1, 00133 Rome, Italy
[c]LTCI, Télécom Paris, Institut Polytechnique de Paris, France
[d]Faculty of Aerospace Engineering, Delft University of Technology, Kluyverweg 1, 2629 HS Delft, The Netherlands

**corresponding author: zwijsen@nrg.eu*

ABSTRACT

A significant aspect of the economic performance and safety of a nuclear reactor involves maintaining the integrity of the fuel rods, which are susceptible to Turbulence Induced Vibrations (TIV) resulting from the axial flow of the coolant. TIV can instigate severe repercussions, including structural damage such as fatigue and wear. TIV can be studied numerically, using Fluid-Structure Interaction (FSI) simulations. However, high-resolution approaches are computationally too expensive to use for complex FSI simulations, while Unsteady Reynolds-Averaged Navier-Stokes (URANS) simulations severely underpredict the displacement amplitudes of the vibrations as they only resolve the mean flow. Evolving from this shortfall, this paper focuses on a recently developed Anisotropic Pressure Fluctuation Model (AniPFM). This model generates a synthetic velocity fluctuations field, which is used to solve for the pressure fluctuations. Using this model, together with URANS, is a possible way to simulate the excitation mechanisms of TIV of fuel rods in a computationally cheaper way. While previous research has highlighted the potential of this model, there are parameters, definitions, and constants whose impacts on the model are not yet fully understood. Therefore, a comprehensive effort is undertaken to fine-tune the model, optimize its performance, improve understanding of it and further validate it. This is done by applying AniPFM to both pure flow and FSI cases, using high-resolution numerical and experimental data as reference and for comparison. With the optimized model, a substantial decrease in average difference from the experimental data is found for the FSI case under consideration, when compared with the unoptimized version of AniPFM.

Keywords: *turbulence-induced vibrations, fuel rods, synthetic turbulence, URANS, pressure fluctuations*

1. INTRODUCTION

Nuclear energy is a very efficient source of power due to its high energy density per unit mass and volume (Lamarsh and Baratta, 2001). This means that a small amount of nuclear fuel can produce a large amount of usable energy. In addition to being a form of electricity generation with very low CO2 emissions, nuclear energy has also made significant progress in terms of technology and applications. As the demand for energy increases and the earth's average temperatures continue to rise (IPCC, 2023), it is necessary to reduce reliance on fossil fuels. While the development of fully sustainable energy solutions is ongoing, nuclear energy will likely play a significant role in meeting our immediate power needs. To ensure the safety of nuclear reactors, all aspects must be carefully controlled and the behavior of each system must be thoroughly studied under all potential conditions.

The coolant liquid, such as water, gas, molten salt, or liquid metal, is an important aspect of nuclear safety, as it is responsible for cooling fuel rods and transporting the heat to the secondary side for power and electricity generation. Fuel rods are submerged in the coolant liquid, which typically flows axially over them to promote efficient cooling. However, this axial flow can also lead to Turbulence Induced Vibrations (TIV) in the fuel rods, which can cause structural damage such as fatigue and wear (Luk, 1993 and Shu et al., 2019). According to IAEA (2019), grid-to-rod-fretting wear (GTRFW), resulting from such vibrations, is the cause of 58% of fuel failures in Pressurized Water Reactors (PWRs) worldwide, while over 70% of all fuel rod leakages in US PWRs are due to Flow-Induced Vibrations (FIV), according to EPRI (2008). It is therefore crucial to consider the effects of TIV on fuel rod integrity in order to ensure the economic performance and safety of the nuclear reactor.

The study of turbulence-induced vibrations in fuel rods has been a topic of interest since the development of nuclear reactors in the 1950s. It has been a cause of numerous incidents (Weaver et al., 2000) and has thus been the focus of many experiments and semi-empirical analyses. These analyses have attempted to establish a relationship between the amplitude of vibration and various parameters such as flow velocity and fluid mass density, as well as structural parameters such as the diameter of the fuel rod, natural frequency, and damping ratio (Basile et al., 1968, Païdoussis, 1969, and Wambsganns and Chen, 1971). However, the results of these studies have shown significant discrepancies between theory and experiment, with semi-empirical relations demonstrating an error of one order of magnitude or more. Additionally, these studies have often only examined a single fuel rod, leading to uncertainty in the extrapolation of these semi-empirical methods to situations involving multiple fuel rods in a bundle.

In recent years, the use of Fluid-Structure Interaction (FSI) simulations for studying fuel rods has gained attention with the increasing availability of computational resources. High-resolution methods such as Direct Numerical Simulation (DNS) and Large Eddy Simulation (LES) can offer accurate predictions. However, their computational demands make them unsuitable for complex FSI simulations. Medium-resolution methods, based on the Unsteady Reynolds-Averaged Navier-Stokes (URANS) approach, have been explored for complex FSI simulations of TIV on fuel rods. URANS-based FSI simulations show good correlation with validation data in terms of frequency and damping ratio, but they show an underprediction of the amplitudes of the displacement as they only resolve the mean flow and hence average out the pressure fluctuations responsible for the fuel rods' vibrations (De Ridder et al., 2013 and DeSantis et al., 2019).

An interesting alternative to modelling TIV is the use of Synthetic Turbulence (ST) models, which attempt to model the velocity fluctuations, and possibly subsequently the pressure fluctuations, instead of solving for them directly through the use of scale-resolving methods. ST models have been applied in several fields within Computational Fluid Dynamics (CFD), such as for constructing the inflow conditions for LES and DNS (di Mare et al., 2006, Castro and Paz, 2013, and Auerswald et al., 2016), for noise modelling (Bailly and Juve, 1999, Billson et al.,2004, and Ewert et al., 2011), particle dynamics modelling (Smirnov et al., 2001), hybrid LES-RANS transition regions (Davidson and Billson, 2006, Laraufie and Deck, 2013, and Shur et al., 2014), modelling of pressure forces on tall buildings (Senthooran et al., 2004), and the modelling of fatigue loading on wind turbines (Kitagawa and Nomura, 2003, and Kleinhans et al., 2009).

Some form of synthetic turbulence modeling has also been used by researchers to assess flow-induced vibrations of important Nuclear Power Plant (NPP) components. Most of this work though focuses on structures subjected to cross-flow, with a large emphasis on Fluid-Elastic Instability (FEI) (Lever and Weaver, 1982, Price and Païdoussis, 1986 and Price, 1995). This work was later also extended to axial flow, though the focus remained predominantly on FEI, instead of looking into TIV (Hassan et al., 2010, El Bouzidi and Hassan, 2015, and Rehman et al., 2023). Some work was done on modeling the structural response due to the turbulence excitation, however, this was either one-way coupled, in which the structural's motion did not change the flow field (Axisa et al., 1990 and Antunes et al., 2015), or predominantly analytical in nature, whereby the flow field is not explicitly resolved (Elbanhawy et al., 2020, and Elbanhawy et al., 2021). Hence, to the authors' knowledge, no two-way coupled TIV simulations involving ST models have previously been performed in which both the flow field and structural displacement are explicitly solved. This though is important if one wants to study the flow field and structural motion in detail in time, instead of focusing mainly on FEI or the stabilitly of the system, and requires reproduce the turbulent velocity field fluctuations.

ST models use different methods to reproduce these velocity fluctuations. One of the first methods to develop synthetic turbulence, and on which a bulk of the methods used today are based, uses the Random Flow Generation (RFG) method. This method uses random Fourier modes and an input energy spectrum to reproduce the velocity fluctuations, and was first proposed by Kraichnan (1970) to generate homogeneous isotropic turbulence. Bailly and Juve (1999) introduced time correlation in Kraichnan's model by including convection and angular frequency terms in the Fourier modes. Senthooran (2004) and Kottapalli et al. (2017) later on slightly modified the model and used it to reproduce pressure fluctuations. Billson et al. (2004), followed a different approach to include convection and time correlation in their model. They first solve an advection equation for the velocity fluctuations, which is subsequently linearly combined with a newly generated velocity fluctuations field to better reproduce time correlation. Additionally, they adjusted the model such that it can be applied to anisotropic turbulence by scaling the isotropic components using the normalized Reynolds stress tensor. One drawback of this scaling is that the divergence-free criterion can only approximately be met (Saad et al., 2017).

Smirnov et al. (2001) proposed a method for simulating inhomogeneous anisotropic turbulence, by scaling the isotropic velocity fluctuations obtained by Kraichnan's method with a tensor obtained through similarity scaling of the Reynolds stress. Since the Reynolds stress and the local time and length scales, used to further scale the fluctuations, vary in space, the method is implicitly inhomogeneous. Smirnov et al.'s method uses a Gaussian energy spectrum as opposed to the modified Von Karman Spectrum. Batten et al. (2004) simplified this method by using Cholesky decomposition instead of using similarity transformations. Huang et al. (2010) modified Smirnov et al.'s method such that any spectrum model could be used. Castro and Paz (2013) later adjusted this method with an improvement of the temporal correlations. Advantage of Castro and Paz' method is that it provides a divergence-free inhomogeneous anisotropic field, and is highly parallelized. Furthermore, the energy spectrum is free of choice and it shows great temperoal and spatial correlation compared to analytical results. Drawback is that the anisotropy is only related to the diagonal Reynolds stress tensor terms, and hence not the off-diagonal terms. Furthermore, it includes several ad-hoc parameters that need to be chosen carefully.

The former drawback was addressed by Shur et al. (2014), who developed an improved version of Adamian and Travin's model (2011), by defining the velocity fluctuations such that the second moment tensor is equal to the Reynolds stress obtained from a URANS simulation, using a Cholesky decomposition. They used a modified version of the Von Karman spectrum, allowing to normalize the amplitudes of the velocity fluctuations. Advantage herefo is that the height of the spectrum becomes irrelevant. For time correlation though, a simple constant convection velocity was used.

Another method used to generate ST is the Digital Filtering (DF) method, first proposed by Klein et al. (2003). In the DF method, velocity fluctuations are obtained by filtering random fluctuations such that prescribed time and space correlations are imposed. While Klein et al. (2003) used filtered random noise, Fathali et al. (2008) used filtered random

fields rather. Xie and Castro (2008) later adjusted Klein et al.'s method to make it more computationally efficient, by using 2D slices and providing a time correlation between them, rather than generating a 3D filtered velocity field. Additionally, they used exponential correlation functions, instead of Guassian functions used previously. Xie and Castro's method was later on made divergence-free by Kim et al. (2013). For time correlation, a similar method to Billson et al. (2004) was used. To get the method to produce a synthetic turbulence field with prescribed Reynolds stresses, a Cholesky decomposition is once more used.

While the end result of Kim et al's method is divergence-free inhomogeneous anisotropic turbulence, there are some drawbacks. The method is designed for uniform Cartesian grids, making it difficult to apply it to FSI cases. One could generate the velocity fluctuations first on such a grid, and then interpolate it to a non-uniform unstructured grid, though this introduces additional uncertainties and computational costs. Another drawback is that it is computationally quite expensive, in particular compared to the RFG methods. Furthermore, the filter is based on a constant integral length scale, whereas the integral length scale typically varies.

Another ST method closely related to the DF methods are Random Particle Mesh (RPM) methods, first proposed by Ewert (2017). It also takes a random variable, which is subsequently filtered to obtain a correlated velocity field. For RPM methods though, the domain is divided into equally sized control volumes, where a particle is assigned to the centre of each volume. Each particle is associated with a random variate and move with their respective local convective velocities. The velocity fluctuations are related to the random variate through a three-dimensional filter function (Hu et al., 2017, Hu et al., 2019). An advantage of this method is that it uses local turbulent length scales and turbulent kinetic energies, meaning it can readily be used for highly non-uniform flow fields. It also allows for implementation of accurate convection and time decorrelation. Its main drawback though is that it is computationally very expensive, especially compared to RFG methods.

Two other ST methods proposed in literature are the Synthetic Eddy (SE) method and Power Spectral Density (PSD) method. The former, first proposed by Jarrin et al. (2006), tries to mimic the representative coherent eddis of turbulent flow by creating a box of eddies of varying length scales and have these convect with the local averaged RANS velocity. Each eddy is given a velocity distribution, and the velocity fluctuations are then determined using the distribution and distance from each eddy. Most recent SE methods were developed by Sescu and Hixon (2012) and Hirai et al. (2019). The difficulty in applying SE methods to FSI problems is that they do not use any energy spectrum as input. Finally, PSD methods are mainly used to predict the power spectral density of pressure fluctuations (Goody, 2004, Rozenberg et al., 2012 and Lee, 2012). They are usually fitted to empirical data and used to calculate surface pressure fluctuations. It is difficulty though to construct a pressure fluctuations time series from the spectrum, in particulat for unsteady flows involving moving boundaries.

The Nuclear Research & consultancy Group (NRG) has been working for several years on developing a synthetic turbulence model to accurately predict TIV of structures subjected to incompressible, axial, single-phase flows. This ST model, called the Pressure Fluctuation Model (PFM), uses the RFG method to generate velocity fluctuations, and is based on the model developed by Senthooran (2004). It has been integrated into the fluid side of NRG's existing framework for FSI simulations (Kottapalli et al., 2017 and Kottapalli et al., 2019). The PFM simulates pressure fluctuations based on URANS data, which are then applied to the fuel rod as an external excitation for the Computational Structural Mechanics (CSM) solver. The FSI simulations using PFM showed promising results with amplitudes of displacement of the same order of magnitude as experimental data, but still lacked the desired level of accuracy (Kottapalli et al., 2019).

To improve the prediction of pressure fluctuations through ST models, a full revision of the model was undertaken, highlighting its shortcomings. Subsequently, following a thorough literature study of ST models, of which a brief summary is found above, a new and improved PFM was developed, which was subsequently named AniPFM (Anisotropic Pressure Fluctuation Model) (Van den Bos et al., 2022 and Zwijsen et al., 2024). Among the many improvements compared to the original PFM, AniPFM allows for the reconstruction of anisotropic Reynolds stresses (hence the name AniPFM), represents only the resolved scales of velocity fluctuations, and incorporates time correlation methods based on turbulence transport. It was validated with two fluid-only cases and one FSI case. On the fluid side, AniPFM showed a better representation of the turbulent kinetic energy near the wall, compared to its previous version. Also in terms of the FSI validation, AniPFM shows much better results than before. While the results are promising, AniPFM needs to be researched further to reduce its uncertainty and understand its dependency on certain model parameters.

The current paper presents work done towards a better understanding and further validation of AniPFM. First, an extensive sensitivity analysis is conducted to investigate the impact of various parameters on the model's performance in a flow-only scenario. Using channel flow statistics obtained from direct numerical simulation, the aniPFM model is further optimized. Next, the performance of this optimized model in capturing axial flow-induced vibration in a practical FSI scenario is studied. The paper is structured as follows. In Section 2, AniPFM is presented in detail. This section also presents the model parameters and modelling choices whose impact on the results are investigated in the remainder of this paper. Subsequently, in Section 3, the numerical framework, in which AniPFM is implemented and which is used to perform fluid-structure interaction simulations, is outlined. Sensitivity studies performed with AniPFM on a fluid-only case are presented in Section 4, while results obtained with AniPFM for an FSI case are discussed in Section 5. Finally, in Section 6, conclusions and future work are listed.

2. DESCRIPTION OF THE ANISOTROPIC PRESSURE FLUCTUATION MODEL

To obtain an expression for the pressure fluctuations, the Reynolds decomposition of the velocity $\mathbf{u} = \bar{\mathbf{u}} + \mathbf{u}'$ and pressure $p = \bar{p} + p'$, with the overline denoting the mean and the prime denoting the instantaneous fluctuation from the mean, are substituted in the incompressible Navier-Stokes equations. When the averaged momentum equation is subtracted from the obtained equation, and the divergence operator is applied, one is left with the following Poisson equation for the pressure fluctuations:

$$\frac{\partial^2 p'}{\partial x_i \partial x_i} = -\rho_f \left[2\frac{\partial \bar{u}_i}{\partial x_j}\frac{\partial u'_j}{\partial x_i} + \frac{\partial^2}{\partial x_i \partial x_j}\left(u_i' u_j' - \overline{u_i' u_j'}\right)\right]. \tag{1}$$

The right-hand side of this equation only depends on the mean velocity $\bar{u}_i$, the Reynolds stress tensor $\overline{u_i' u_j'}$ and the instantaneous velocity fluctuations u_i'. The first two can be obtained from a URANS simulation. In order to obtain the pressure fluctuations, which are responsible for the motion of structures subjected to axial flow, the velocity fluctuations need to be constructed.

2.1 Dimensionless velocity fluctuations

As illustrated by Eq. (1), in order to obtain the desired pressure fluctuations, velocity fluctuations $\mathbf{u}_t(x,t)$ that are a function of space and time are needed. Hereto, as a first step, dimensionless velocity fluctuations $\mathbf{w}_t(x)$ are constructed that are only a function of space, using the following Fourier decomposition:

$$\mathbf{w}_t(x) = \sqrt{6}\sum_{n}^{N} \sqrt{q_n}[\boldsymbol{\sigma}_n \cos\left(\mathbf{k}_n \cdot \mathbf{x} + \varphi_n\right)], \tag{2}$$

where, q_n is the mode amplitude, $\boldsymbol{\sigma}_n$ is the direction vector, $\mathbf{k}_n$ is the wavenumber vector, and φ_n is a random phase shift with a uniform distribution. The subscript n denotes the n-th Fourier mode, with in total N modes. The multiplication factor of $\sqrt{6}$ comes from the fact that a one-sided signal (i.e. positive wavenumbers) is used to construct the nondimensional velocity fluctuations and that the squared average of $\mathbf{w}_t(\mathbf{x})$ must be equal to the Kronecker-delta. The generation of dimensionless velocity fluctuations is necessary in order to introduce anisotropy later on.

In order to generate $\mathbf{w}_t(x)$, expressions for the mode amplitude, mode direction vector and its wavenumber vector are needed. The mode amplitude q_n specifies the amount of energy contained in mode n. The total amount of energy of all the modes is equal to the local Turbulent Kinetic Energy (TKE), obtained from the URANS simulation. The distribution of the local turbulent kinetic energy among the modes is given by a TKE spectrum. In AniPFM, the modified Von-Kármán energy spectrum $E(k)$ is used (Shur et al., 2014):

$$E(k) = \frac{(k/k_e)^4}{[1 + 2.4((k/k_e)^2)]^{17/6}} \exp\left(-\left(12\frac{k}{k_\eta}\right)^2\right) f_{cut}. \tag{3}$$

Here k is the wavenumber under consideration, k_e is the wavenumber at which the energy spectrum has its maximum, k_η is the Kolmogorov wavenumber and f_{cut} is a filter that cuts off the spectrum at wavenumbers that cannot be resolved by the mesh. This filter and the range of wavenumbers included in the model is discussed further below, in Section 2.2. The resulting energy per mode is normalized to get the desired dimensionless velocity fluctuations:

$$q_n = \frac{E_k(k_n)\Delta k_n}{\sum_n^N E_k(k_n)\Delta k_n}, \tag{4}$$

with $E_k(k_n)$ the modified Von-Kármán energy spectrum evaluated at k_n.

For the wavenumber vector, the following definition is used, which is also illustrated in Figure 1:

$$\mathbf{k}_n = k_n[\sin\theta_n \cos\psi_n, \sin\theta_n \sin\psi_n, \cos\theta_n], \tag{5}$$

where θ_n, ψ_n and $\varphi_n$are random variables with distributions given by:

$$P(\psi_n) = \frac{1}{\pi}, \quad P(\varphi_n) = \frac{1}{2\pi}, \quad P(\theta_n) = \frac{1}{2}\sin(\theta_n). \tag{6}$$

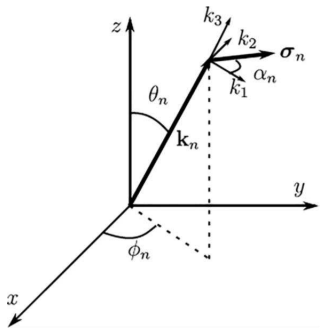

Figure 1: Wave vector geometry of the n-th Fourier mode.

Finally, the wavenumber direction vector is determined from the wavenumber vector. Based on continuity, it can be found that $\mathbf{k}_n \cdot \boldsymbol{\sigma}_n = 0$. To achieve this, $\boldsymbol{\sigma}_n$ is defined as the normalized cross-product between the random vector $\boldsymbol{\zeta}_n = [\sin\theta_\zeta \cos\psi_\zeta, \sin\theta_\zeta \sin\psi_\zeta, \cos\theta_\zeta]$, and the wavenumber vector:

$$\boldsymbol{\sigma}_n = \frac{\boldsymbol{\zeta}_n \times \mathbf{k}_n}{|\boldsymbol{\zeta}_n \times \mathbf{k}_n|}. \tag{7}$$

2.2 Wavenumber range and cut-off filter

In order to properly generate the velocity fluctuations, a correct wavenumber range should be used, spanning modes that can be represented on the used mesh. The mesh should be constructed such that the most relevant modes can be captured. As the used energy spectrum, given by Eq. (3), spans the full wavenumber range up to the Kolmogorov wavenumber, which a URANS mesh cannot resolve, a cut-off filter f_{cut} is used, given by (Shur et al., 2014):

$$f_{cut} = \exp\left(-\left[\frac{4\max(k - 0.9k_{cut}, 0)}{k_{cut}}\right]^3\right), \tag{8}$$

where $k_{cut} = 2\pi/l_{cut}$, with l_{cut} the cut-off length. This cut-off length corresponds to the highest wavenumber included in the Fourier decomposition, mode *N*, through $k_{end} = \frac{3}{2}k_{cut}$ and is mesh-dependent. Two different expressions for l_{cut} are tested too. The first uses the local grid size dimensions h_y, h_z and h_{max} and the local cell distance to the wall d_w (Shur et al., 2014):

$$l_{cut} = 2\min\{[\max(h_y, h_z, 0.3h_{max}) + 0.1d_w], h_{max}\}, \tag{9}$$

while the second one is based on the local cell volume V_{cell}:

$$l_{cut} = 2V_{cell}^{1/3}. \tag{10}$$

The starting wavenumber k_{start}, corresponding to the first mode, is given by:

$$k_{start} = \max\left[\min\left(k^*_{start}, \frac{1}{2}k_e\right), \frac{2\pi}{l_{user}}\right], \tag{11}$$

where k_e corresponds to the wavenumber at which the used energy spectrum has its peak, l_{user} is a used defined length scale and k^*_{start} is a conservative estimate for the largest eddy length scale in the domain:

$$k^*_{start} = \frac{\epsilon}{\max(\|\mathbf{u}\|^3)}. \tag{12}$$

Here, ϵ is the eddy dissipation rate. Eq. (11) ensures the starting wavenumber is smaller than the peak wavenumber. This TKE peak wavenumber is given by $k_e = 2\pi/l_e$. Hence to define k_e, an expression for l_e, the corresponding length scale, is needed. Following Shur et al. (2014), two different expressions for l_e have been implemented:

$$l_e = C_l l_t = C_l \frac{\mathrm{TKE}^{3/2}}{\epsilon}, \tag{13}$$

with TKE the local (cell) turbulent kinetic energy, ϵ the local (cell) turbulent dissipation rate and C_l a calibration factor, and

$$l_e = \min(2d_w, C_l l_t)\,. \tag{14}$$

Previously, Eq. (13) with $C_l = 3$ was used (Zwijsen et al., 2024). However, this combination was calibrated for isotropic turbulence, while fluid-structure interaction is inherently anisotropic. Hence, in this work, both expressions are evaluated, using different values for the calibration factor.

Having defined the wavenumber range from k_{start} to k_{end}, the range is divided in N intervals. This results in $N + 1$ edge wavenumbers, which are logarithmically distributed as follows:

$$\tilde{k}_n = k_{start} \cdot e^{\gamma i}, \tag{15}$$

with γ given by:

$$\gamma = \frac{\log(k_{end}/k_{start})}{N}. \tag{16}$$

Then, the wavenumbers are defined as the logarithmic middle of interval n, i.e., $k_n = \tilde{k}_{n+1/2}$. The variable Δk_n as needed in Eq. (4) is found through $\Delta k_n = \tilde{k}_{n+1} - \tilde{k}_n$. With this, the dimensionless velocity fluctuations can be generated.

2.3 Anisotropic velocity fluctuations

Before scaling the dimensionless velocity fluctuations generated as outlined in Section 2.2, time-dependency is included first. Two phenomena contribute to the time correlation of the velocity field, namely the convection of the turbulent eddies and the decorrelation due to production and dissipation. This time dependency is introduced using the following two-step method (Billson et al., 2004):

$$\frac{\partial \mathbf{v}_t^{m-1}}{\partial t} + \overline{u_j} \frac{\partial \mathbf{v}_t^{m-1}}{\partial x_j} = 0, \tag{17}$$

$$\mathbf{v}_t^m(\mathbf{x}, t) = a\mathbf{v}_t^{m-1}(\mathbf{x}) + b\mathbf{w}_t^m(\mathbf{x}). \tag{18}$$

Here, $\mathbf{v}_t^{m-1}$ are the non-dimensional velocity fluctuations generated at time step $m - 1$, and $\overline{u_j}$ is the Reynolds-averaged velocity as produced by URANS. In the first step, i.e. Eq. (17), the dimensionless velocity fluctuations are convected with the local URANS velocity. Then, in the second step, a new solution $\mathbf{v}_t^m(\mathbf{x}, t)$ is calculated from a combination of the (convected) previous solution $\mathbf{v}_t^{m-1}(\mathbf{x})$, and a newly generated field $\mathbf{w}_t^m(\mathbf{x})$. The coefficients a and b are defined by:

$$a = e^{-f_\tau \Delta t/\tau}, \quad b = \sqrt{1 - a^2}, \tag{19}$$

with τ the characteristic timescale determined from the URANS simulation, and f_τ a modification factor for fine-tuning the correlation. More on this modification factor later.

Finally, the space-time-dependent velocity fluctuations $\mathbf{v_t}(\mathbf{x}, t)$ obtained after solving Eqs. (17) and (18) are scaled as follows, such that they replicate the desired Reynolds stresses and, hence, introduce the desired anisotropy:

$$\mathbf{u}_t(\boldsymbol{x}, t) = a_{ij}\mathbf{v_t}(\mathbf{x}, t), \tag{20}$$

with a_{ij} the Cholesky decomposition of the Reynolds stress tensor R, given by (Shur et al., 2015):

$$a_{ij} = \begin{bmatrix} \sqrt{R_{11}} & 0 & 0 \\ \dfrac{R_{21}}{a_{11}} & \sqrt{R_{22} - a_{21}^2} & 0 \\ \dfrac{R_{31}}{a_{11}} & \dfrac{(R_{32} - a_{31}a_{21})}{a_{22}} & \sqrt{R_{33} - a_{31}^2 - a_{32}^2} \end{bmatrix}. \tag{21}$$

For the Cholesky decomposition a, it follows that $a^T a = R$. Thus, if $\langle \mathbf{v}_t(\mathbf{x},t)^2 \rangle = \delta_{ij}$, it follows that $\langle \mathbf{u}_t(\mathbf{x},t)^2 \rangle$ is the Reynolds stress tensor. From this it can be concluded that $\mathbf{v}_t(\mathbf{x},t)$ must indeed be isotropic, and the squared-averaged components must be equal to unity.

With the above-described method, the AniPFM can reconstruct anisotropic Reynolds stresses. For flows such as channel flows, linear eddy viscosity models produce isotropic Reynolds stresses. In order to improve the accuracy of these models, a correction is used to transform the isotropic tensor into an anisotropic tensor, based on the nonlinear eddy viscosity model of Wilcox (1993) determined for a flat-plate boundary layer:

$$\overline{u'u'} = \frac{8}{9}k, \quad \overline{v'v'} = \frac{4}{9}k, \quad \overline{w'w'} = \frac{6}{9}k. \tag{22}$$

2.4 Pure convective velocity fluctuations

In order to introduce convection and turbulent production and dissipation into the velocity fluctuations, Eqs. (17) and (18) are solved. This so-called Convection & Exponential Correlation (C&EC) method requires solving an additional differential equation. While numerically cheap, it can cause numerical dissipation due to the treatment of the advection term. Therefore, as an alternative, convection has also been implemented directly in Eq. (2). This method, called Pure Convection (PC), algebraically generates the velocity fluctuations that are a function of both space and time through:

$$\mathbf{v}_t(\mathbf{x},t) = \sqrt{6}\sum_n^N \sqrt{q_n}[\boldsymbol{\sigma}_n \cos(\mathbf{k}_n \cdot (\mathbf{x} - \bar{\mathbf{u}}t) + \varphi_n)], \tag{23}$$

where $\bar{\mathbf{u}}$ is the local mean velocity as solved by the URANS simulation. With this method, the random variables are no longer indirectly a function of time, but are generated during the first iterations and subsequently stored.

3. FSI SIMULATIONS FRAMEWORK

AniPFM is implemented in the NRG-FSIFOAM framework used at NRG, to perform fluid-structure interaction simulations. This framework uses a partitioned approach. The finite volume OpenFOAM solver is utilized to solve the governing fluid equations using a PIMPLE algorithm, which is a combination of the classical PISO and SIMPLE algorithms. The fluid mesh is deformed using the displacementLaplacian solver in OpenFOAM. This solver uses a Laplace equation to determine how the mesh should deform based on the displacement of a moving boundary. For the turbulence cases, URANS is used with the $k-\omega$ SST turbulence model. Other turbulence models were tested, though they either gave similar results at higher computational costs (Explicit Algebraic Reynolds Stress Models (EARSM), such as Hellsten EARSM (Hellsten, 2004) and Wallin & Johansson EARSM (Wallin and Johansson, 2000)), or gave poorer results (standard k-ε). Input from URANS is used in AniPFM to generate the pressure fluctuations, via the mean velocity field, TKE and modeled Reynolds stress tensor. These fluctuations will act as an excitation mechanism on the structure.

On the other hand, the governing equations for the solid problem are solved using the finite element approach implemented in the Deal.II library (Alzetta, 2019). Linear finite element approximation is used to semi-discretize the governing equations in space, and the θ-method is employed for time integration. The fluid and solid solvers are coupled through the preCICE library (Bungartz et al., 2016) for solving FSI problems, with radial basis functions used to consistently map displacements and stresses between the two meshes. A partitioned, parallel implicit coupling solver is used to solve the FSI problem, with quasi-Newton acceleration methods, specifically the IQN-ILS method (Degroote et al., 2009). The NRG-FSIFOAM framework is schematically depicted in Figure 2.

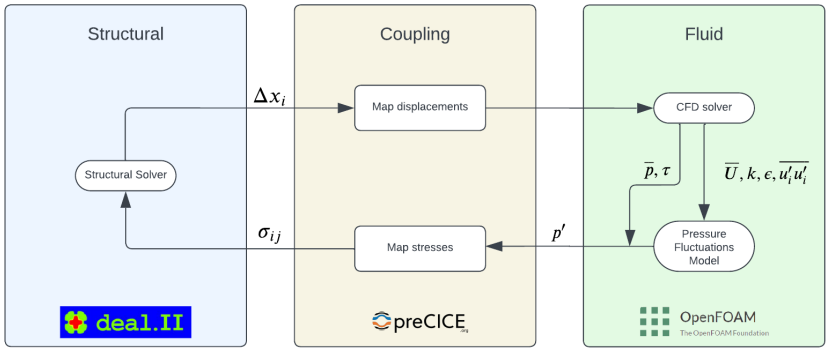

Figure 2: Sketch of NRG-FSIFOAM framework with AniPFM included.

4. ANIPFM OPTIMIZATION

AniPFM, as described above in Section 2, contains various parameters that need to be specified in order to run it successfully.These parameters include the number of modes used in Eq. (2), the seed of the random number generator used to generate the random variables of Eq. (5), the calibration factor C_l of Eq. (13) used to determine the TKE peak wavenumber and the modification factor f_τ of Eq. (19) used in the C&EC scheme. Additionally, AniPFM has two different implementations for the cut-off length, Eqs. (9) and (10), for the TKE peak length scale, Eqs. (13) and (14), and for the time correlation of the velocity fluctuations, Eqs. (17) and (23). Educated choices were made for these parameters and options during initial testing of the model. However, as it was observed that the model is sensitive to some of the choices made, a proper sensitivity testing is needed. Results hereof are described and shown in this section, through simulations of Turbulent Channel Flow (TCF). By applying it to a widely studied flow-only case, a thorough validation of the model can be done, thereby demonstrating in detail the model's functioning, capabilities, and shortcomings. The validation will be done both quantitatively, looking at a wide range of parameters and statistics, and qualitatively. The latter illustrates the differences with standard URANS approaches, and similarities with scale-resolving methods.

4.1 Turbulent channel flow case

The case of TCF was chosen due to its simplicity and the high availability of DNS reference data. The DNS chosen for validation is that of Abe et al. (2001). These researchers performed a DNS study on the Reynolds-number dependence on pressure fluctuations in TCF. Their highest Reynolds number is $Re_\tau = 640$, and thus this is the one chosen to test AniPFM. This DNS was selected because it provided data on the mean flow characteristics, such as velocity profiles and Reynolds stresses, as well as other quantities, such as spectral information regarding pressure and velocity. A sketch of the TCF case is shown in the left of Figure 3. In the TCF, the flow is between two parallel plates, as shown in Figure 3, where $L \gg \delta$ and $b \gg \delta$. L and b are large enough so that the flow in the edges can be considered uncorrelated. This allows one to take a smaller section in the middle of this larger channel and use periodic boundary conditions in the streamwise and spanwise directions. The flow is statistically homogeneous in these directions which means that the mean flow is only dependent on the wall-normal direction, y.

As mentioned in Section 3, for the simulations, the k-ω SST turbulence model is used. A backward time scheme (BDF2) is applied, offering second-order accuracy in time. The time step is constrained by the CFL number, capped at 0.5. For the convergence of the governing equations, an absolute scaled threshold of 10^{-6} is set for all equations, including the pressure fluctuations equation. Periodic boundary conditions are used in the spanwise and streamwise directions, while no-slip conditions are used for the wall. Additionally, a momentum source is used in the streamwise direction to ensure the friction velocity is the same as from Abe et al. (2001).

The AniPFM settings used in this section are summarized in Table 1. The presented results are obtained starting with a precursor steady-state URANS simulation, which is run until all residuals are converged. The converged solution is used to initialize the flowfield of an unsteady simulation using AniPFM, which is subsequently run for 300 seconds (equivalent to roughly 12 flow-throughs). This was found to be enough for having converged Root Mean Square (RMS) pressure fluctuations for all the meshes considered. As mentioned before, the channel flow is only statistically inhomogeneous in the wall-normal (y) direction, and thus unless mentioned otherwise, the results presented have been averaged in the statistically homogeneous directions. Furthermore, when one-dimensional spectra are displayed, they are

averaged over the other homogeneous direction. For example, if a spectrum is shown in the streamwise direction, it is averaged over the spanwise direction.

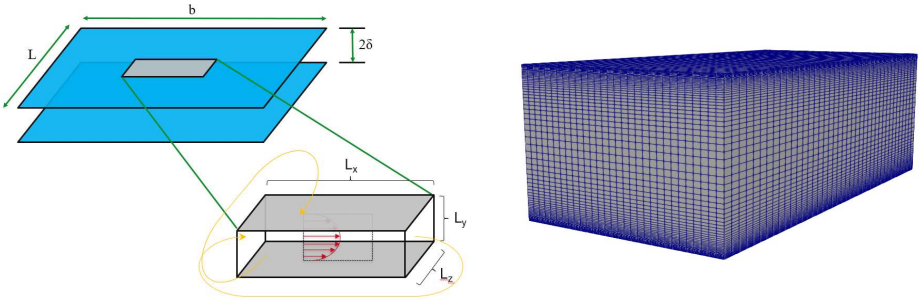

Figure 3: Left: sketch of turbulent channel flow case, and right: example mesh used for the simulations.

Table 1: Overview of AniPFM parameters used in each section.

Section	# modes	Rand. Seed	Time. Corr	f_τ	l_e	C_l	Cut-off
4.2	256	Default (0)	C&EC	25	Eq. (13)	3.0	Eq. (9)
4.3	256	Default (0)	C&EC, PC	25	Eq. (13)	3.0	Eq. (9)
4.4	Varying	Default (0)	C&EC, PC	25	Eq. (13)	3.0	Eq. (9)
4.5	256	Varying	C&EC, PC	25	Eq. (13)	3.0	Eq. (9)
4.6	256	Default (0)	C&EC, PC	Varying	Eq. (13)	3.0	Eq. (9)
4.7	256	Default (0)	C&EC	25	Eqs. (13) & (14)	3.0	Eq. (9)
4.8	256	Default (0)	C&EC	25	Eq. (13)	Varying	Eqs. (9)
4.9	256	Default (0)	C&EC	25	Eq. (13)	Varying	Eqs. (9) & (10)
4.10	256	Default (0)	C&EC	25	Eq. (13)	Varying	Eqs. (9) & (10)

4.2 Mesh sensitivity

Before testing the sensitivity of AniPFM to the aforementioned parameters and modelling choices, a mesh sensitivity study is done. The simulation domain is set at dimensions of $6\delta \times 2\delta \times 3\delta$, with δ representing the channel half-height. The mesh sizes in different directions are $N_x \times N_y \times N_z$, where these values are varied resulting in different mesh resolutions. The grid is evenly spaced in the x and z directions, but expands geometrically from the wall towards the mid-channel plane in the y direction. All the different meshes are wall resolved such that $y^+ \leq 1$. Having a wall-resolved mesh is important in order to correctly capture the Root-Mean Square (RMS) pressure fluctuations at the wall, as will be shown momentarily. Details of the meshes used for the mesh sensitivity study are listed in Table 2, while the coarsest mesh used is visualized on the right of Figure 3.

Table 2: Settings used for the mesh sensitivity study.

Mesh	N_x	N_y	N_z	N_{cell}
M1	40	80	30	96,000
M2	50	96	40	192,000
M3	80	112	60	537,600
M4	120	128	90	1,382,400

Before presenting quantitative results, Figure 4 shows some qualitative results obtained using the coarsest mesh. The instantaneous streamwise velocity (top left) and pressure fluctuations (bottom left) both look as one would expect, that is, zones of higher and lower values are present, though no clear pattern is discernable. Higher values are generally found at the walls, due to the stronger turbulence production there. These higher values are better visible when looking at the mean-squared fluctuation fields, shown in the right of the same figure. The highest values are clearly found near the wall, with lower values found in the middle of the channel. Not much variability is found in the streamwise direction due to

the homogeneity of the channel flow case in this direction. The variability still present is a result of a lack of (time) averaging, and hence would disappear with longer simulation time. To speed up the averaging process, for the remainder of this paper, all data are collapsed onto a single profile as a function of the wall-normal direction, thereby making use of the homogeneity in the two other directions. It is important to note here that scale-resolving methods, such as LES and DNS, would reproduce similar instantaneous fields as shown in the left of Figure 4. URANS on its own, on the other hand, without the used AniPFM, would not reproduce any of the shown fluctuations.

The RMS pressure fluctuations as a function of the the wall-normal coordinate for the different meshes are compared with DNS data in Figure 5. A clear mesh convergence can be observed, with the difference between curves reducing as the mesh resolution increases. An increase in resolution is also seen to lead to higher pressure fluctuations due to the greater amount of resolved turbulence kinetic energy. Moreover, the finer meshes capture the increase in turbulent production in the buffer layer more accurately. When set against DNS data, the overall shape of the curves is quite similar, with a few key differences: an underestimation of the increase of p'_{RMS} in the buffer layer, a reduced prediction of pressure fluctuations away from the wall, and an overestimation of the RMS pressure fluctuations close to the wall for $y^+ < 10$. In particular, this overprediction of the pressure fluctuations close to the wall may be a concern, as it is anticipated that the pressure fluctuations at the wall drive for a large part the vibrations of structures subjected to axial flow, which is the main application case of AniPFM. Hence it will be a primary focus to try to understand which of the aforementioned model choices and settings cause AniPFM to overestimate them, and hence what combination gives the best predictions.

Figure 5 also illustrates why it is important to have a wall-resolved mesh. Because only then will the p'_{RMS} at the wall be in the flat part of the profile, found for $y^+ < 5$. For higher y^+ values, it will either be in the peak or the decreasing section of the curve.

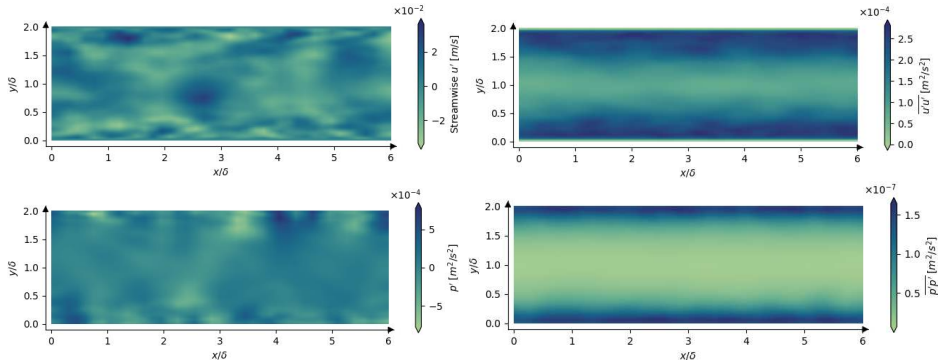

Figure 4: Plots of streamwise velocity (top) and pressure fluctuations (bottom) on a vertical slice through the middle of the channel, with left: instantaneous fields and right:Mean-squared fields.

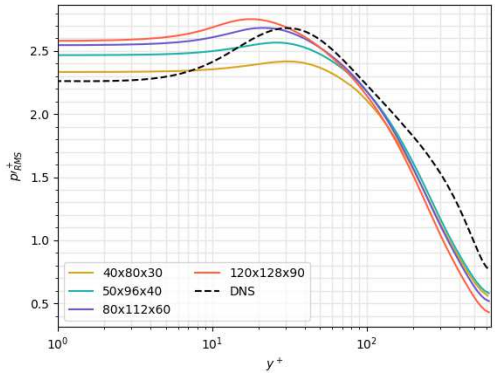

Figure 5: RMS pressure fluctuations as a function of the wall-normal coordinate for different meshes.

Figure 6 shows the comparison of the normal Reynolds stresses as functions of y^+ between DNS (dashed curves), AniPFM (solid curves) and the input RANS (with Wilcox correction, dotted curves) for the coarsest (left) and finest (right) meshes. Blue lines are for the $\overline{u'u'}$ Reynolds stress component, orange lines for the $\overline{v'v'}$ component and green curves for the $\overline{w'w'}$ one. As can be seen, and is well known, RANS strongly underpredicts the streamwise component of the Reynolds stress, at least when the Wilcox correction is used to divide the TKE among the different components. As the RANS Reynolds stress is used as input for AniPFM, it also strongly underpredicts the streamwise component. A better match is found for the spanwise and wall-normal directions by both RANS and, therefore also, by AniPFM.

Comparing the coarsest and finest meshes, it becomes clear that the increase in mesh resolution increases the amount of turbulent kinetic energy retained by the model, with this increase most noticeable close to the wall. In particular, comparing with the input URANS Reynolds stresses, it becomes clear that as the mesh resolution increases, the Reynolds stresses of AniPFM become closer to the input ones.

What is interesting to note here is that when looking at the pressure fluctuations equation, Eq. (1), for the current TCF case, which resembles annular flow along a cylinder quite a bit, and for which statistics only depend on the wall-normal coordinate, the pressure fluctuations only depend on the wall-normal component of the Reynolds stress, through the term $\frac{\partial \overline{v'v'}}{\partial y^2}$. This term is larger for the finest mesh near the wall than for the coarsest mesh, which explains why larger RMS pressure fluctuations are found near the wall with the finest mesh. Additionally, Figure 6 also demonstrates the unique anisotropic feature of the model, as, due to the use of the Wilcox correction given by Eq. (22), it generates separate Reynolds stress components, instead of a single value of the turbulent kinetic energy coming from a URANS solver.

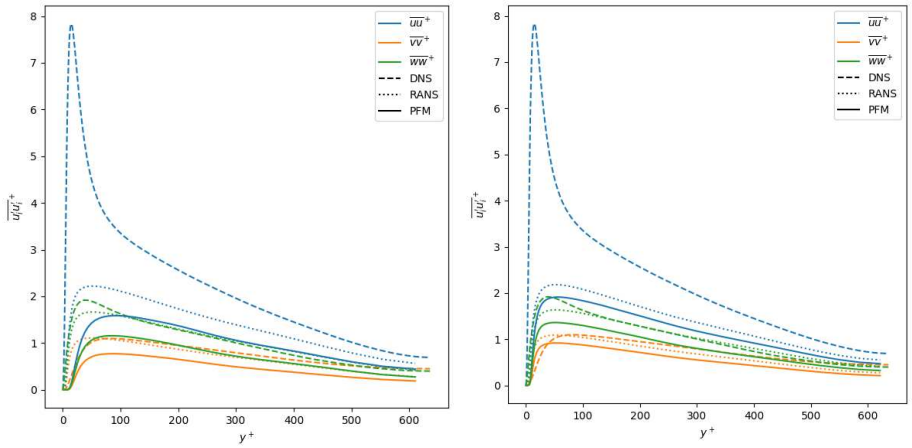

Figure 6: Reynolds stresses as function of the wall-normal coordinate for the coarsest (M1, left) and finest (M4, right) meshes, compared with the underlying URANS simulation and DNS results.

To speed up the computations, unless mentioned otherwise, the coarsest mesh presented above was used for the simulations performed in the upcoming sections. The conclusions taken from the results are considered valid and generalizable for finer meshes in terms of trends but not absolute values. The generalization to finer meshes is done in Section 4.10.

4.3 Time correlation method

Two different methods are implemented in AniPFM to take the time correlation of the velocity fluctuations into account, viz. C&EC through Eqs. (17) through (19) and PC as given by Eq. (23). Both methods have their advantages and drawbacks. C&EC incorporates both convection and turbulence decorrelation due to production and dissipation, thereby more realistically reproducing turbulent flow. Its main drawbacks are that additional equations (compared to pure convection) need to be solved, increasing slightly simulation time, and the fact that these equations introduce numerical diffusion. This numerical diffusion could decrease the magnitude of the velocity fluctuations near the wall and thus decrease the magnitude of the pressure fluctuations. This potential problem is not present with the PC method, as convection is calculated algebraically. Its drawback is that it does not consider turbulence decorrelation, hence the only time dependency of the generated velocity field is through advection.

To illustrate the difference in the behaviour of the two methods in time, Figure 7 shows instantaneous velocity fluctuation fields using PC (top) and C&EC (bottom) at t = 0.0 s (left) and t = 5.0 s (right). As can be seen, the two methods generate nearly identical initial fields, with there only being some slight local differences. After five seconds of simulation time, the fields look completely different. Using PC, the initial field is simply convected with the local mean velocity, resulting in a similar velocity fluctuation field as the initial field. This is not the case when C&EC is used, giving a vastly different field at t = 5.0 s than the initially generated one. This is a direct result of the implemented combination of convection and exponential time correlation, given by Eqs. (17) – (19), and which is important to correctly recover the time correlation of the generated velocity and pressure fluctuations.

4.4 Number of modes

The number of modes N used in the Fourier series to generate the velocity fluctuations is one of the input parameters of the model. To investigate its dependency, simulations with both time correlation methods (PC and C&EC) were performed with the number of modes varying from 64 to 2048. The RMS pressure fluctuations as function of y^+ are shown in Figure 8. As can be seen, the pure convection method (left figure) is very dependent on the number of modes; while the curves collapse for higher y^+, for the lower y^+ values there is a large difference in the magnitude of the RMS of pressure fluctuations. Furthermore, the method shows no signs of convergence, nor is there a clear trend in the curves, at least not with the number of modes analysed here. On the other hand, the right plot of Figure 8 shows that the C&EC method is independent of the number of modes used. This observed difference is caused by the fact that the C&EC method generates a new velocity fluctuation field at every time step, as input for Eq. (18), while the PC method simply convects the initial field, as was illustrated in Section 4.3. Generating a new field also means a new set of random numbers is generated, removing any dependency on the used set of random numbers.

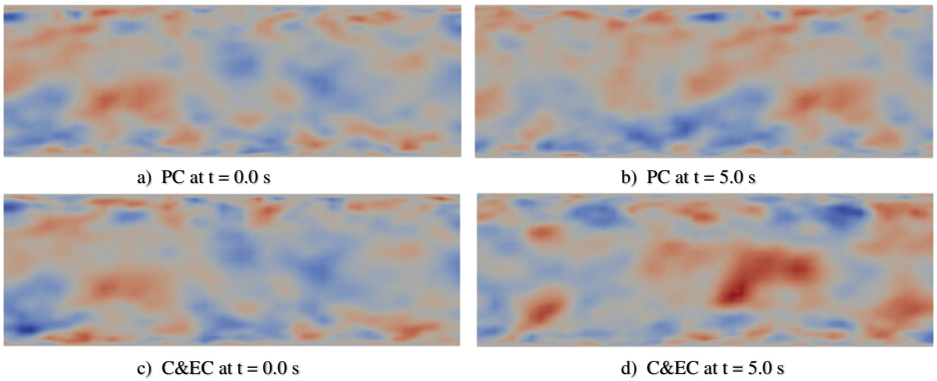

Figure 7: Instantaneous velocity fluctuation fields using PC (top) and C&EC (bottom) at t = 0.0 s (left) and t = 5.0 s (right).

A solution would be to increase the number of modes further, thereby using more random numbers. However, this will increase the computational time significantly, as shown in Figure 9. Additionally, the C&EC methods is only slightly more expensive computationally than the PC method.

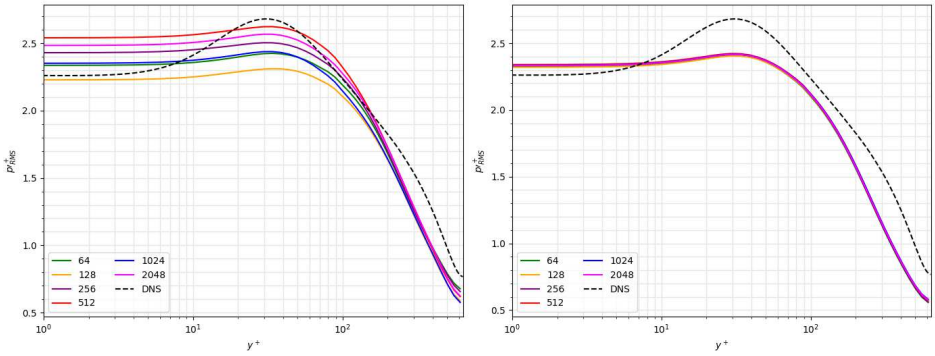

Figure 8: RMS of the pressure fluctuations as a function of the wall-normal coordinate for various number of modes using PC (left) and C&EC (right)

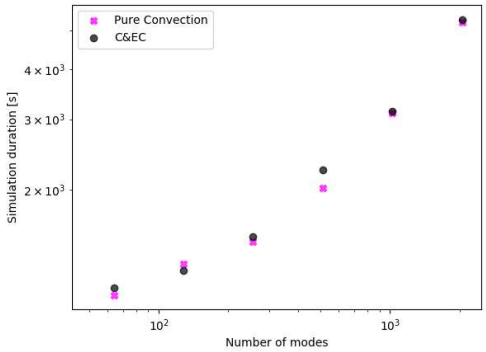

Figure 9: Simulation time for different numbers of modes using both time correlation methods.

4.5 Random number generator seed

As it was seen in Section 2.1, the wave number vector $\mathbf{k}_n$ and the auxiliary vector $\boldsymbol{\zeta}_n$, which is part of the expression for the direction vector $\boldsymbol{\sigma}_n$, are obtained through sines and cosines of random variables. These random variables are generated by a pseudo-random number generator (RNG). Although RNGs generate numbers that seem random, most of them are actually deterministic in nature (hence 'pseudo'); given the same seed, they will produce the same sequence of numbers every time. This property can be useful in situations where reproducibility is desired, such as during sensitivity testing of the model to specific parameters and modeling choises. As such, the random seed is one of the user inputs of the model.

While reproducibility is desired, the obtained results should depend minimally on the seed of the RNG. To investigate if this is the case for AniPFM, several simulations were performed using different seeds. This was done using the PC method and C&EC methods. Figure 10 shows the RMS of the pressure fluctuations at $y^+ = 10$ for both methods using different seeds. There is a strong dependence on the seed using the PC method. Using the C&EC method this dependence is much smaller. Quantifying this dependency, in the case of PC, on average, the difference between using different random seeds and the baseline seed (considered 0 here) is roughly 5%. On the other hand, for C&EC simulations, this value is 1.37%. Furthermore, using C&EC, this value will decrease if the simulation time is increased, as more fields, using new random numbers, are added every time step, averaging out the observed differences. This is not the case when using the PC method, which retains the initial set of random numbers, without adding new ones. This also makes the PC method more prone to outliers with relatively high, or low, RMS pressure fluctuations.

This reduced dependency of the C&EC method further illustrates it is a more robust method than PC.

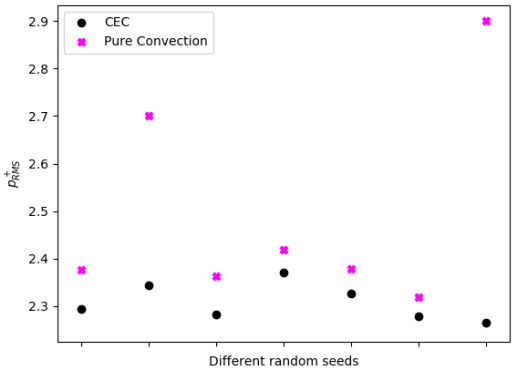

Figure 10: RMS of the pressure fluctuations at y+ = 10 for different random seeds using both PC & C&EC.

4.6 Modification factor f_τ

Previously, for the initial testing of AniPFM, a modification factor $f_\tau = 17$, was used for simulations involving the C&EC method. This value was chosen following Billson et al. (2004). However, this value was based on the simulation of a 3D jet, which is significantly different from wall-bounded flow such as turbulent channel flow or flow around a fuel rod. Hence, impact of the value of this parameter on the obtained results should be investigated.

Figure 11 shows the influence of the value of the modification factor on the Reynolds stresses (left), and on the RMS pressure fluctuations (right), both plotted as functions of the wall-normal coordinate in wall units. For comparison, simulation results for the Reynolds stresses using PC are also included in the left figure. As can be seen from the figures, the lines converge to each other when the value of f_τ is increased. For the Reynolds stresses, for a value above 50, hardly any difference can be discerned, while for the RMS pressure fluctuations, this already is the case for $f_\tau \geq 25$. From Eq. (19) it can be seen that a higher value of f_τ means more weight is put onto the newly generated velocity fluctuations field and less on the convected one. This also means numerical dissipation as a result of solving the advection equation of the velocity fluctuations, viz. Eq. (18), resulting in a decrease of resolved TKE, is less pronounced for higher f_τ values.

As in particular the pressure fluctuations are important for FSI simulations, and to not fully eliminate the convected part to obtain updated velocity fluctuations, it was decided to use $f_\tau = 25$ in future FSI simulations.

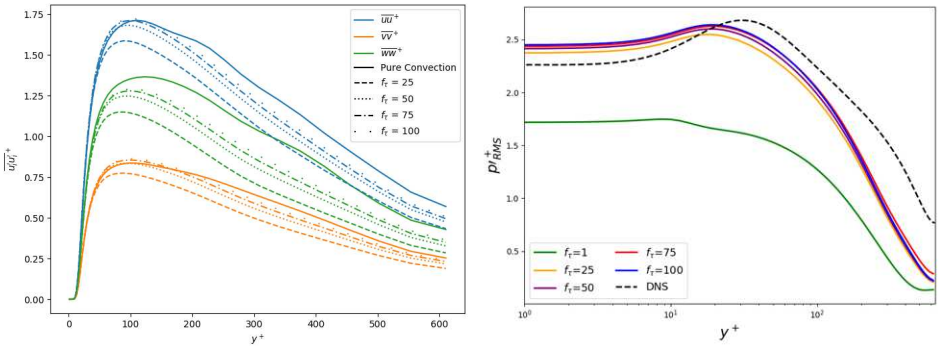

Figure 11: Influence of the value of the modification factor f_τ on the normal Reynolds stresses (left) and the root-mean square pressure fluctuations (right) as functions of the wall-normal coordinate.

To further illustrate the influence of the value of the modification factor, and to assess the physicality of the generated turbulence, a quadrant analysis of the Reynolds shear stresses was performed. The concept of such a quadrant analysis was introduced by Wallace et al. (Wallace et al., 1972). They categorized products of velocity fluctuations into four distinct groups based on the signs: Q1 $(+u', +v')$, Q2 $(-u', +v')$, Q3 $(-u', -v')$, and Q4 $(+u', -v')$. These groups later became known as the quadrants of the Reynolds shear stress plane. The Q2 and Q4 motions correspond to the ejection and sweep events, where ejections correspond to a movement away from the wall and backwards and sweep events

correspond to a down and front movement. Wallace termed the Q1 and Q3 motions as "outward" and "inward" interactions, respectively (Wallace, 2016).

As an example as well as comparison, Figure 12 a) shows a quadrant analysis of a turbulent channel flow DNS at $Re_\tau = 180$ at a location of $y^+ \approx 20$ performed by Kim et al. (Kim et al, 1987, public database). As confirmed by the figure, in the buffer layer, with $10 < y^+ < 30$, the events that are most common are Q2 and Q4 events, ending up with a joint Probability Density Function (PDF) that looks like a normal distribution stretched in the diagonal between Q2 and Q4.

In order to perform the quadrant analysis of simulations with AniPFM, multiple probes were placed at a location of $y^+ = 10$ throughout the domain. From these probes, the velocity fluctuations were retrieved and averaged across the various points, ending up with one final vector with the size of the number of measured time steps. The resulting joint PDFs between the streamwise and wall-normal velocity fluctuations for PC, C&EC with $f_\tau = 1$ and C&EC with $f_\tau = 25$ are shown in Figure 12. Joint PDFs obtained for higher correlation factors gave very similar patterns as obtained with $f_\tau = 25$ and hence are not shown. The stretching observed in the reference analysis is clearly visible with the C&EC method, giving a strong emphasis on Q2 and Q4 events. This is, in particular, the case for $f_\tau = 25$ (and higher values). The stretching is much less visible with the PC method. The joint PDF obtained with AniPFM is less flat though than the reference DNS, which can partly be explained by looking at Figure 6. There it can be seen that the difference between the $\overline{u'u'}$ Reynolds stress component and the $\overline{v'v'}$ component is much larger for the DNS than for AniPFM, indicating that the u' versus v' ratio will also be larger for DNS. This is further amplified by the fact that the reference DNS plot is for $y^+ \approx 20$, while the AniPFM plots are for $y^+ = 10$, where the relative differences are smaller.

Overall, the C&EC method performs well, especially with correlation factors of 25 or higher, while the pure convection method does not align as closely with DNS data.

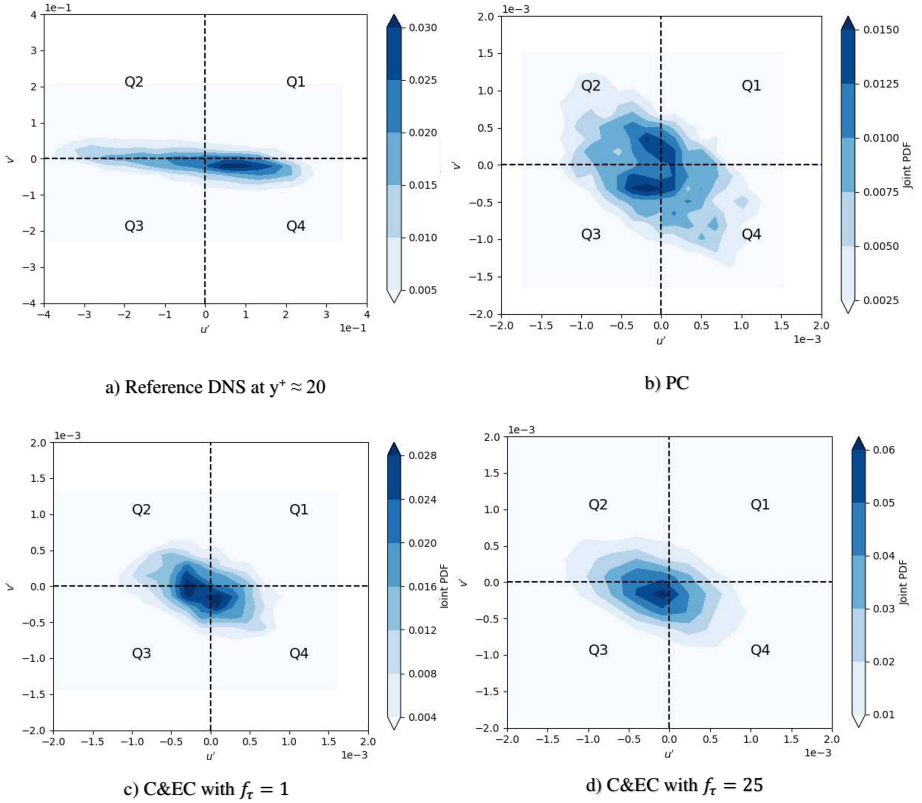

a) Reference DNS at $y^+ \approx 20$ b) PC

c) C&EC with $f_\tau = 1$ d) C&EC with $f_\tau = 25$

Figure 12: Joint PDF of u' and v' with a) reference DNS at $y^+ = 19.2$ (Kim et al., 1987), b) for PC, c) for C&EC with $f_\tau = 1$, and d) for C&EC with $f_\tau = 25$, all at $y^+ = 10.0$.

4.7 TKE peak length scale

Currently, AniPFM contains two expressions for the TKE peak length scale, viz. Eq. (13) and (14), following the work by Shur et al. (2014). The first of these two expressions is based on the local (cell) turbulent kinetic energy, while the second one also takes the local distance to the wall into account.

Figure 13 shows the RMS pressure fluctuations as a function of y^+ for the two different definitions of l_e mentioned earlier, using $C_l = 3$ in line with previous work, as well as for $2d_w$. The last one is also included to understand the role of the minimization function. As the figure shows, the curves of $\min(2d_w, C_l l_t)$ and $2d_w$, which lies below the former, collapse, which means that $2d_w$ is always smaller than $3l_t$ for TCF. The only reason Shur et al. (2014) still chose this approach is because they use their zonal RANS/LES not only on TCF but also on other cases, for which $2d_w$ is not always smaller than $3l_t$. For wall bounded flows, under consideration here, it is found to be always smaller. Furthermore, as can be seen, the expression based on the wall distance vastly underpredicts the RMS pressure fluctuations at the wall. Hence, from now on, the focus will be on the definition of l_e that is based on the local (cell) turbulent kinetic energy, viz. Eq. (13).

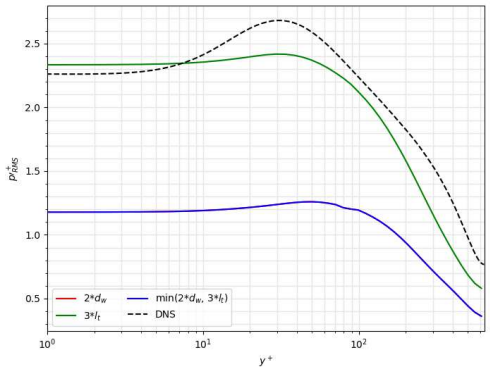

Figure 13: RMS pressure fluctuations along the wall-normal coordinate for different definitions for l_e.

4.8 Calibration factor C_l

In all simulations so far $C_l = 3$ was used, as suggested by Shur et al. (2014). However, this factor was calibrated for isotropic turbulence, while the case under consideration posesses anisotropy. Hence, this factor also needs further investigation. Figure 14 shows the effect of lowering the value of C_l has on the RMS pressure fluctuations. As can be seen, a lower value of the calibration factor leads to lower RMS pressure fluctuations at the wall. In fact, when $C_l = 2.85$ is used, the RMS pressure fluctuations at the wall are nearly identical to the reference DNS values, at least when Eq. (9) is used for the cut-off length scale.

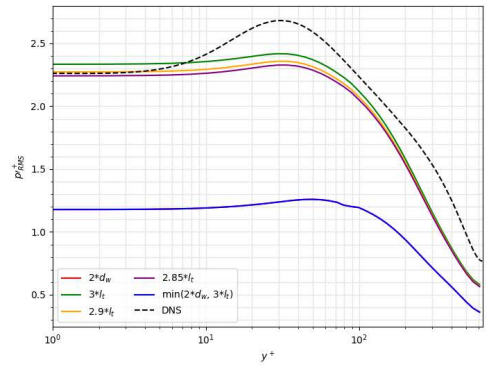

Figure 14: RMS pressure fluctuations along the wall-normal coordinate for different values of C_l, using Eq. (9) for the cut-off length scale.

It is hypothesized that the observed influence of C_l on the RMS pressure fluctuations is a result of its impact on the TKE spectrum through Eq. (3). A lower value of C_l results in a lower TKE peak length scale, which on its turn results in a higher TKE peak wavenumber. As the shape of the TKE spectrum is fixed and given by Eq. (3), and the total area underneath the TKE spectrum is given by the local TKE coming from the URANS model, a rightward shift in the TKE peak wavenumber should be accompanied by an overall drop of the TKE spectrum, meaning the energy contained in each mode is slightly lower. And slightly less energetic velocity fluctuations result in lower pressure fluctuations, as a result of Eq. (1).

4.9 Cut-off length scale

Finally, the effect of the choice of the cut-off length scale is investigated. Two different expressions have been implemented, viz. the one based on Shur et al. (2014), Eq. (9), from hereon named Shur cut-off, and one based on the cubic root of the local cell volume, Eq. (10), from hereon named cubic cut-off.

The determination of the cut-off length scale is important as it controls, along with the mesh resolution, how much energy of the energy spectrum is resolved. However, this task is not trivial as the cut-off length and the energy spectrum are represented with scalars, whereas in reality, the cut-off length varies locally in the three dimensiones. This is most noticeable in areas where the mesh is highly non-cubical, such as near the wall, where cells generally have high aspect ratios. Namely, at the wall, the cell height in the wall-normal direction is much smaller than the length in the span- and streamwise directions. Thus, a much smaller cut-off length could be used in the wall-normal direction than in the span- and streamwise direction. If the cut-off length of the wall-normal direction was used, the resolved energy in the span- and streamwise direction would be overestimated, whereas if the cut-off length of the span- or streamwise direction were used, the resolved energy in the wall-normal direction would be underestimated. This could potentially be resolved by using separate TKE spectra for each of the three velocity fluctuation components. However, that would add another level of complexity to the model. Furthermore, it may not be needed, as shown below.

An example of the cut-off length for the different methods is shown in Figure 15. As can be seen, the cubic cut-off gives a cut-off length more than twice as small as the Shur cut-off near the wall. Near the mid-channel the values are closer, as the mesh cells are generally less stretched. From this, it can be expected that the RMS pressure fluctuations will be lower when using the Shur cut-off, as less energy is resolved. This is confirmed in Figure 16, showing the RMS pressure fluctuations as a function of the wall-normal coordinate using the cubic cut-off. When looking at the plot with $C_l = 3.0$ the RMS pressure fluctuations are clearly much higher than those obtained with the Shur cut-off using the same value for the calibration factor, as shown in Figure 14.

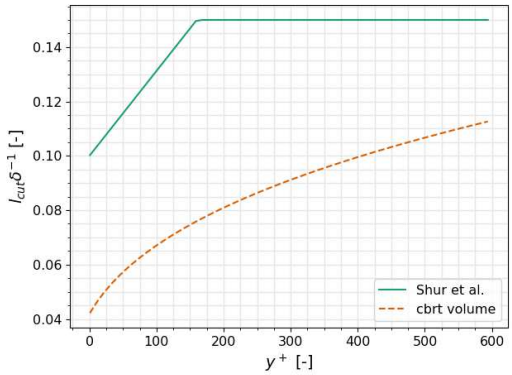

Figure 15: The cut-off length scale for both the Shur cut-off expression and the cubic one.

As was done for the Shur cut-off, it is possible to calibrate the value of C_l used with the cubic cut-off in order to better match the RMS pressure fluctuations at the wall. Results of this calibration are also shown in Figure 16. As expected a much smaller value is needed for the cubic cut-off than for the Shur cut-off, as the cubic cut-off cuts the energy spectrum at a higher wavenumber than the Shur cut-off. Comparing both cut-offs with the optimised coefficients, the cubic cut-off shows a better overall shape as it shows a more pronounced peak than the one with Shur cut-off.

To further assess the difference between the two expressions for the cut-off length, Figure 17 shows the frequency power spectra of the wall pressure fluctuations for the two cut-off length definitions using the optimized values for the calibration factor C_l. Since Abe et al. (2001) had no data on the frequency spectrum, the DNS data used here for comparison is taken from Hu et al. (2006). The experimental data is from Brungart et al. (1999). The DNS data from Hu et al. (2006) is at $Re_\tau = 720$, while the simulations are at $Re_\tau = 640$. Moreover, the experimental data from Brungart et al. (1999) was performed at $Re_\theta = 1120$, with θ equal to the momentum thickness, while the simulations performed are at $Re_\theta \approx 800$. However, for this range of Reynolds numbers, it was shown that, if properly non-dimensionalised, the frequency spectra for the different Re_τ or Re_θ overlap (Hu et al., 2006).

To obtain this frequency spectra, multiple probes were placed in the domain at a height equal to the height of the center of the first cell in the y direction. These probes sample the pressure fluctuations with a certain constant frequency. Subsequently, the spectra are computed and in turn averaged over the different probes, resulting in one final spectrum. Both methods, using the optimized C_l, give reasonable results at lower frequencies, in particular using the cubic cut-off, which overlaps the DNS results. This was not the case for $C_l = 3.0$, with both methods overpredicting the lower frequencies, especially using the cubic cut-off, in line with earlier results.

While the spectrum of the cubic cut-off follows almost a straight line across the entire range of angular frequencies, the spectrum of the Shur cut-off shows a slight drop for higher frequencies. While this drop is not alike the DNS one, it

is still more similar. The absence of the strong drop at higher frequencies for both cut-off methods is probably a result of the absence of actual turbulence production and decay in the model, but instead it being represented through the C&EC method of Eqs. (17) and (18). While it seems to work well for lower frequencies, it overpredicts the power of higher frequencies.

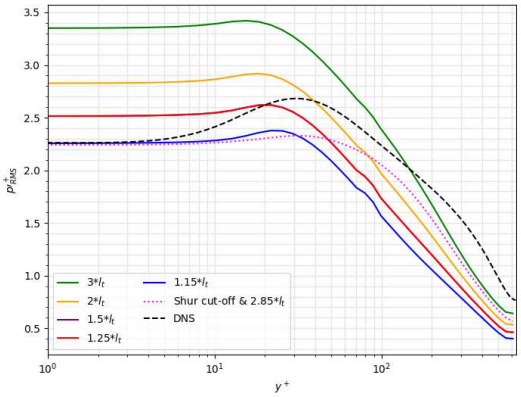

Figure 16: RMS pressure fluctuations along the wall-normal coordinate for different values of C_l, using Eq. (10) for the cut-off length scale.

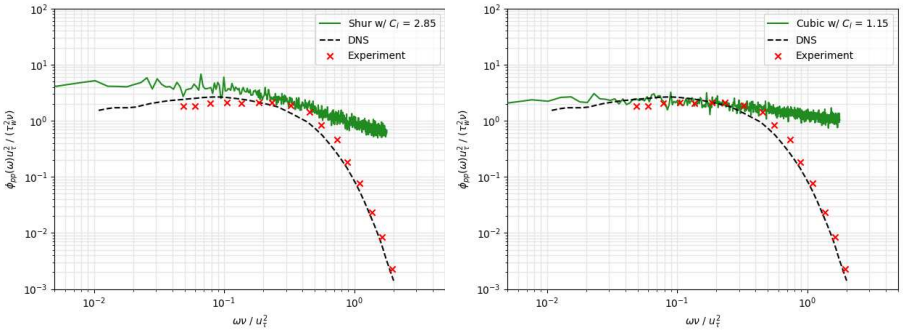

Figure 17: Frequency power spectra of the wall pressure fluctuations for Shur cut-off with $C_l = 2.85$ (left) and for cubic cut-off with $C_l = 1.15$ (right).

In addition to the above comparison in the time-frequency domain, a comparison is also done in the wavenumber domain. Abe et al. (2005) performed a DNS study of Reynolds number dependence of pressure fluctuations in TCF, in which they have data for wavenumber power spectra of pressure fluctuations at the wall for $Re_\tau = 640$. This data will be compared with AniPFM results. Figure 18 shows the streamwise wavenumber power spectra of the wall pressure fluctuations. The results are quite spurious, which probably is a result of the coarse mesh used. Comparing the two methods, the plots look very similar with both showing the drop in the power spectra for higher wavenumbers, that in the frequency domain was not present in the cubic cut-off. For the higher wavenumbers, both methods show the DNS curve quite well. At lower wavenumbers, the Shur cut-off remains more or less flat, similar to the DNS, while the cubic cut-off has a slight increase with increasing wavenumber, before dropping at high wavenumbers. As said, though, both methods reasonably recover the DNS curve.

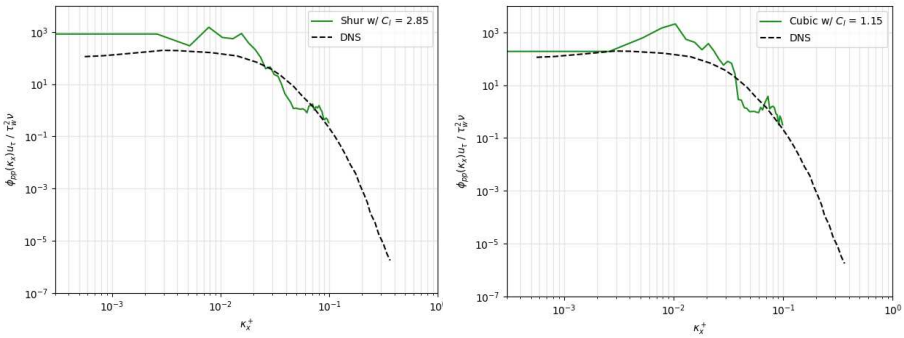

Figure 18: Streamwise wavenumber power spectra of the wall pressure fluctuations for Shur cut-off with $C_l = 2.85$ (left) and for cubic cut-off with $C_l = 1.15$ (right)

4.10 Refined mesh

So far, all sensitivity studies were performed using the coarse mesh, in order to speed up the computations. However, as was shown in Section 4.2, results were not converged for this mesh. Therefore, it is important to assess results for the fine, converged mesh, using the preferred values and choices as found above, such as C&EC for the time correlation, a modification factor $f_\tau = 25$, and the expression for the TKE peak length scale based on the local turbulent kinetic energy, i.e., Eq. (13). However, a calibrated C_l coefficient is still needed for the converged meshes. Figure 19 shows the RMS pressure fluctuations along the wall-normal coordinate for the different meshes, using the Shur cut-off and with $C_l = 2.0$. As can be seen, for that value the converged mesh gives a good match with DNS data for the RMS pressure fluctuations at the wall. Additionally, as expected from Figure 5, a lower value for this empirical constant is needed for the fine mesh compared to what was previously found for the coarsest mesh. The same approach was applied to simulations using the cubic cut-off and a $C_l = 0.6$ was found as the optimal value. While these values are set for this specific flow case and mesh, it is interesting to check how they perform for FSI simulations. This will be investigated in the next section.

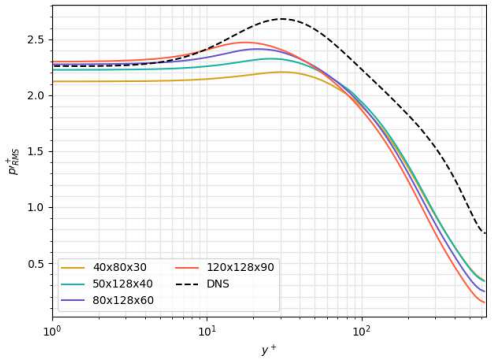

Figure 19: RMS pressure fluctuations as a function of the wall-normal coordinate for various meshes, using the Shur cut-off and $C_l = 2.0$

5. FSI SIMULATION

The previous chapter focused on AniPFM applied to a pure flow case, viz. turbulent channel flow. The model is developed to be applied for axial-flow induced vibrations, in particular to simulate turbulence-induced vibrations of fuel rods. Hence, this chapter presents results of AniPFM used for FIV simulations. In this chapter, first the chosen experiment

will be presented, along with previous numerical setups used by other researchers. Next, the used simulation setup is described. And finally, the results are presented.

5.1 Experiment & previous numerical work

To see how the optimized AniPFM performs for FSI simulations, it was applied to the flexible brass beam experiment in turbulent water flow performed by Chen & Wambsganss (1972). This experiment was chosen because it closely mimics turbulence-induced vibrations found in nuclear reactors, and has been used by other researchers in the past for validation purposes (De Ridder et al., 2013, Kottapalli et al., 2019, Nazari et al., 2019, and Zwijsen et al., 2024). It consists of a brass beam with diameter D_i = 0.0127 m and length L = 1.19 m placed inside a cylinder with a diameter D_o = 0.0254 m through which water flows. A sketch of the numerical replication of this experiment can be seen in Figure 20. The beam has a mass density of 8400 kg/m^3, giving a density ratio of $\rho_s/\rho_l = 8.4$, and a Young's modulus of E = 107 GPa. The Poisson's ratio was not specified, but a value of 0.33 is used for the simulations. The beam is clamped on both sides. The experiment was conducted with various mean inlet velocities, ranging from 8 to 33 m/s, resulting in Reynolds numbers between 101,600-419,100.

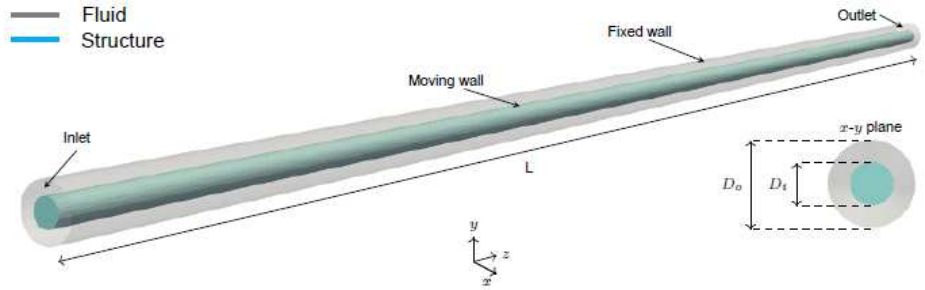

Figure 20: Fluid and solid domains of the brass beam FSI case.

The experiment has been replicated numerically by several researchers. De Ridder et al. (2013) used FSI simulations with an initial displacement of the beam to calculate the natural frequency of the fundamental mode. They solved fluid dynamics using a URANS k − ω SST turbulence model and structural mechanics using a commercial finite element solver, Abaqus. The IQN-ILS method was used to couple the solvers. The simulations were conducted at speeds of 10-30 m/s. Modal frequencies were calculated for all three flow cases, with and without pre-stress.

Furthermore, De Ridder (2015) also performed wall-resolved LES simulations without FSI. However, the root-mean squared amplitude of the beam was calculated by computing the force spectrum from the LES data, and using this with an analytical relation that was introduced by Chen &Wambsganss (1972). In order to reduce the computational cost, the rod was not simulated at its full length, but instead a smaller rod was used with a length/diameter ratio of 10. For this case, the mesh used had 76.8 million cells. Extrapolating this for a full length rod, it would yield roughly 720 million cells just for the fluid side. These simulations were solely performed at 10 m/s.

Kottapalli et al. (2019) used a similar FSI approach to De Ridder et al. (2013), though also simulated the rod without initial displacement using a pressure fluctuation model (PFM, predecessor of AniPFM). Similarly, a partitioned approach was taken, where the IQN-ILS coupling method was used to couple a URANS k −ω CFD simulation with a finite element structural solver. This was done at 10m/s as well.

Finally, Nazari et al. (2019) simulated the experiment with a partitioned approach, using both URANS and LES for the calculations of the fluid domain. The fluid domain was modelled with the k −ω SST turbulence model for the URANS case, while a finite element solver was used to solve the structural domain. It is not clear what coupling method was used. In the case of the LES simulation, the Dynamic Smagorinsky-Lilly model is used to model the sub-grid stress tensor.

5.2 Simulation setup

The framework outlined in Chapter 3 is used to perform the simulations. All walls are set to no-slip walls. At the inlet, a uniform inlet velocity is used, in agreement with the aforementioned numerical work on this case (De Ridder et al., 2013 and Kottapally et al., 2019). Tests using a fully developed flow at the inlet showed that the assumption of a uniform inlet velocity had only a marginal effect on the results, with a difference in natural frequency found of less than 0.05%, and a difference in damping ratio of 1-2%. In addition to the uniform velocity, at the inlet, 5% turbulence intensity and 0.1 cm as turbulent length scale are used. The effect of these settings were studied by De Ridder et al. (2013), who found them to have minimal impact on the results of URANS-based simulations. From preliminary tests this was

confirmed. The flow is fully developed for the majority (roughly 90%) of the domain, and here the kinetic energy profiles are independent of the inlet conditions. This also holds for the pressure fluctuations; in the developed flow region, they are shown to be independent of the kinetic energy at the inlet. Only near the inlet is a variation noticeable; however, the impact of this region on the structural vibration is hypothesized to be considerably less than the developed flow region of the domain. As for the outlet, a zero-pressure boundary condition is used.

The outer steel cylinder is fixed, meaning its inner wall serves as a wall boundary for the fluid. The inner brass beam is modelled as a moving wall, clamped at both ends. A linear elastic solver is used for the brass beam. This is valid when the relative displacements $A_{RMS}/L \ll 1$, which, based on the experimental displacement values, is true for the case under consideration.

The fluid meshes are all wall-resolved. A mesh sensitivity study for a pure CFD case showed that 40 elements in the tangential direction are enough to get converged results. The mesh discretization in the axial direction it is changed to analyse the effect on the results, see below. The same structural mesh from Zwijsen et al. (2024) is used here as well, which was chosen following a mesh convergence study. This means the structural mesh has 25 elements in the x-y plane, and 50 elements in the axial direction, hence 1250 elements in total. Figure 21 (left) shows a front view of the fluid and structural meshes. Quadratic elements are for the structural mesh. Regarding time marching schemes, second-order methods are used for both fluid and structural solvers.

Due to the small density ratio, an implicit coupling scheme is used, namely IQN-ILS. Local radial basis functions are used for data mapping at the fluid-structure interface. These are used because due to the quadratic elements, the structural mesh in the axial direction is quite coarse, thus a higher-order mapping method is necessary. It was found that global radial basis functions take too much computational effort for fluid grids with more than 32,000 interface faces, thus local radial basis functions are used. It was found that by using a support radius that encapsulates 5 elements of both the fluid and the structural mesh, the difference in FSI results is negligible in comparison to global radial basis functions, while reducing the computational cost.

In order to run the FSI simulations, first, steady state fluid–only simulations are run. These are stopped when the residuals are converged, after which the flow field is used to initialize an unsteady simulation (fluid only also) using AniPFM. This is then run for 10 seconds (roughly 84 flow passes through the domain). This simulation is, in turn, used to initialize the fluid model in the FSI simulation, which is run for an additional 10 seconds or longer if the RMS of the displacements are not fully converged yet.

In the following sections, the results of the FSI simulations are presented. Simulations using the two time correlations, PC and C&EC, are once more compared, as well as using the two definitions for the cut-off length, using both $C_l = 3.0$ as the calibrated values. Lastly, a comparison is made between the optimized version of AniPFM and experimental results, and with other researchers' numerical work of this same case.

A summary of AniPFM's parameters used in each section of this chapter is presented in Table 3. When not mentioned otherwise, the used mesh is $50 \times 40 \times 300$.

Table 3: Overview of AniPFM parameters used in each section.

Section	# modes	Rand. Seed	Time. Corr	f_τ	l_e	C_l	Cut-off
5.3	256	Default (0)	C&EC, PC	25	Eq. (13)	3.0	Eq. (9)
5.4	256	Default (0)	C&EC	25	Eq. (13)	2.0 & 0.6	Eqs. (9) & (10)
5.5	256	Default (0)	C&EC	25	Eq. (13)	2.0	Eq. (9)

5.3 Time correlation method

Simulations have been performed with both time correlation methods, using various random seeds and the number of cells in the axial direction, and using an inlet velocity of 10 m/s. Results hereof for the RMS displacement A_{RMS} are presented in Figure 21 (right). Several observations can be made from these results. First of all, when comparing the results of the simulations using different seeds of the random number generator (for $50 \times 40 \times 300$ mesh), it can be seen that the seed hardly has any impact on the results when using the C&EC method, while a large spread in A_{RMS} values is visible when using PC. This is in line with what was found for TCF, and underscores the robustness of the C&EC method.

The spread in A_{RMS} values when using the PC method makes is also hard to find mesh convergence. When using the C&EC method though, similar RMS displacements are found using the two finest meshes. Hence, the mesh with 50 radial elements, 40 tangential ones and 300 elements in axial direction will be used henceforth.

In order to have a more qualitative comparison between the PC and C&EC time correlation methods, polar plots of the center of the beam are shown in Figure 22. To obtain these plots, kernel density estimation (KDE) was applied to estimate the probability density function of the data. This allows one to illustrate the density of the points, meaning the frequency it occurs at a particular displacement. There is a clear difference in the shape of the polar plots of the two time correlation methods; while with C&EC the displacement seems to be independent of the orientation, there seems to be a clear preference in displacement direction using the PC method, resulting in larger displacements in one direction than in

the other. This is most likely due to the randomly generated initial field having an orientation that gives rise to a preferential displacement direction. As this field is not modified anymore but just algebraically convected, this preferential displacement direction will not change anymore. This is not the case with C&EC, due to decorrelation of previously generated fields and the generation of new fields each time step. This hence further illustrates the lack of randomness of the PC method that was observed previously.

Considering that the case is axisymmetric, a preferred displacement direction should not occur, making the C&EC once more the preferred time correlation method to be used.

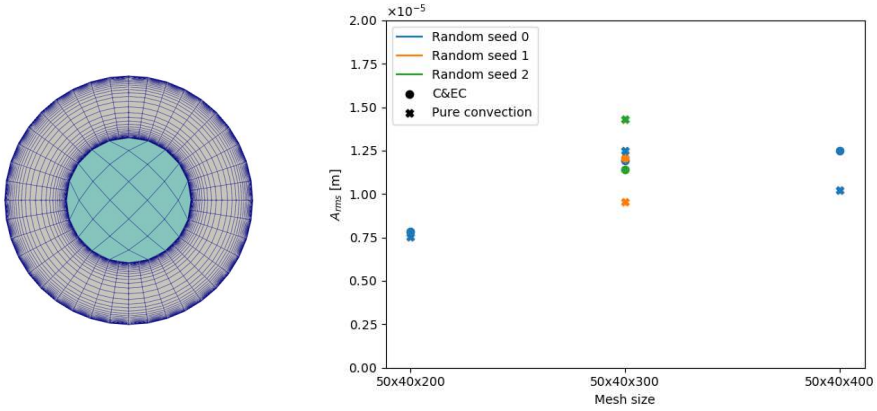

Figure 21: Front view of solid and fluid meshes (left) and comparison of the RMS of the displacement amplitude at the center of the beam for different meshes and time correlation methods (right).

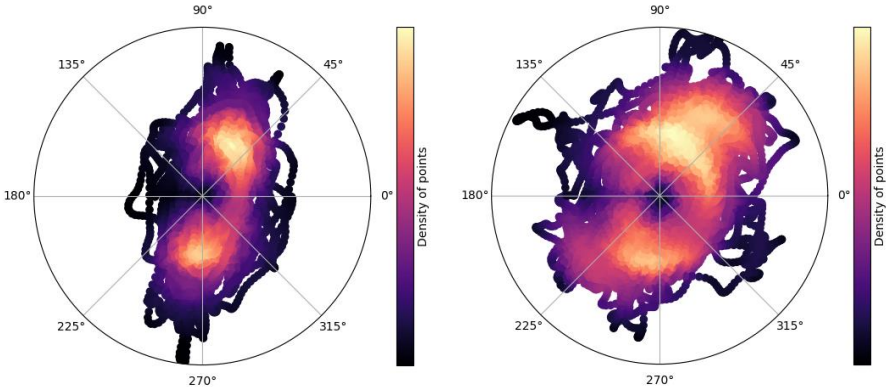

Figure 22: Polar plots of the displacement in the center of the beam for the PC (left) and C&EC (right) time correlation method. Colors indicate the frequency the beam's center is found at a particular displacement.

5.4 Cut-off length scale and calibration factor C_l

For the TFC, it was found that the calibration factor C_l could be adjusted such that the RMS pressure fluctuations at the wall obtained with AniPFM would match the reference DNS values. The idea is that these pressure fluctuations are responsible for the structural movement, and hence dictate the beam's amplitude of displacement. To verify this, FSI simulations of the brass beam are performed, using both cut-off length scale expressions, and using both the baseline and calibrated C_l values. The baseline corresponds to $C_l = 3.0$ and the calibrated versions correspond to the optimal values found in Section 4.10, viz. $C_l = 2.0$ for the Shur cut-off and $C_l = 0.6$ for the cubic cut-off.

Table 4 shows the resulting RMS amplitudes of displacement obtained for an inlet velocity of 10 m/s. The findings confirm the validity of the initial hypothesis. As can be seen clearly, lowering the calibration factor to match the wall RMS pressure fluctuations indeed results in a much better match of the RMS amplitude. It is worth noting here that even though the calibration was done for a pure flow case, using a converged mesh, the same values of C_l also give good predictions for FSI simulations, using once more a converged mesh, at least for the case under consideration.

Table 4: RMS amplitude of displacement for different cut-off length scale expressions and calibration factor values.

Cut-off method	**C_l value**	**A_{RMS} [m]**
Experiment	[-]	6.0e-6
Shur	3.0	1.13e-5
	2.0	7.16e-6
Cubic	3.0	1.61e-5
	0.6	7.26e-6

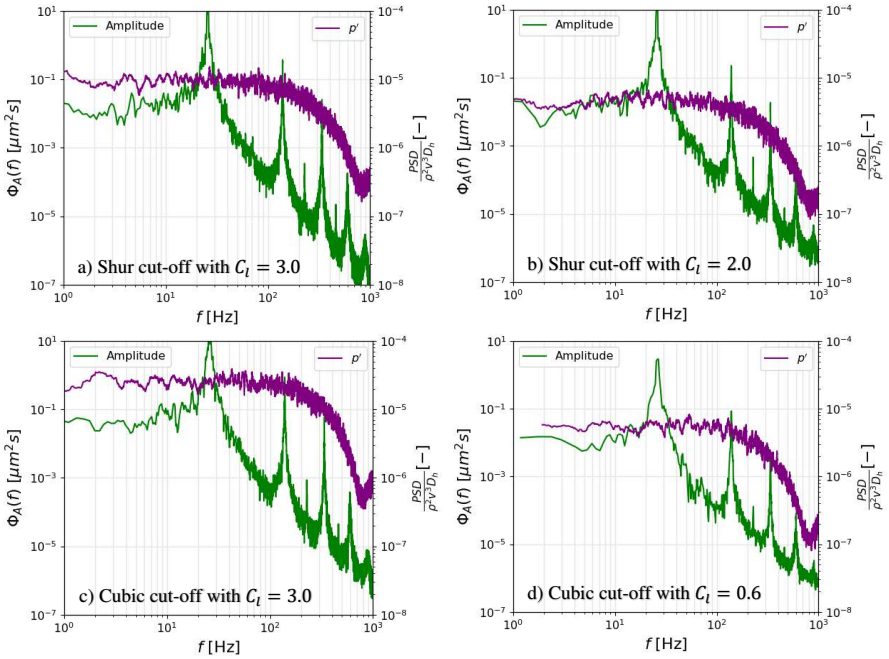

Figure 23: Pressure fluctuations and displacement amplitude spectra for different cut-off length definitions.

To further illustrate the influence of C_l on the results, Figure 23 displays the pressure and amplitude power spectra for the two cut-off definitions, for their baseline and calibrated versions. First, by looking at the different pressure spectra, it is clear that indeed the reduction in the amplitude of displacements is associated with a lower power of the pressure fluctuations. Additionally, the difference in the magnitude of pressure fluctuations between Shur and cubic cut-off is clear, as it was seen for TCF. Moreover, the calibrated versions of the different cut-off definitions show very similar pressure spectra, and also very similar A_{RMS}, indicating that both cut-off expressions can be used, given that they are properly calibrated.

Looking at the amplitude spectra, all cases give similar results, with the main difference being a downward shift for the calibrated C_l values. In terms of shape they appear the same. This is expected as the various peaks correspond to the different frequencies of vibration of the structure, and this is not expected to change due to a change in cut-off expression or C_l value. The first peak, which corresponds to the natural frequency is found to be $f_n = 27$ Hz by the current FSI framework, whereas the experimental reported value is 28 Hz (Chen & Wambsganns, 1972). This slight difference is in line with other numerical researcher's work.

5.5 Results comparison

The sensitivity tests performed on both the TCF and the brass beam FSI case have demonstrated the superior performance of the C&EC method over the PC method. Furthermore, besides giving better and more realistic results, the former method can also be run with fewer modes, with N = 256 being sufficient, and shows the desired insensitivity to the random number generator. Hence the C&EC method is the preferred method for FSI simulations. Additionally, it is suggested to use $f_\tau = 25$ and Eq. (13) for the TKE peak length scale, along with Eq. (9) for the cut-off length scale, with $C_l = 2.0$. These choices give better results for the RMS pressure fluctuations and power spectra, particularly in the important region close to the structure's wall.

FSI simulations using the the above listed values and model choices are performed for flow velocities of 10, 20 and 30 m/s. The found RMS displacements of the beam for various mean flow velocities are shown in Figure 24 with black dots (denoted as Calibrated AniPFM FSI). For comparison, also the experimental results (green dots) and those obtained by Kottapalli et al. (2019) and Zwijsen et al. (2024, denoted as Previous AniPFM FSI), who both used older versions of (Ani)PFM, and by De Ridder et al. (2013), who performed an LES on a rod about nine times shorter than the experimental one, are plotted. As can be seen, the found RMS displacements are very close to the experimental ones, and the optimized AniPFM clearly gives improved results compared to the earlier versions of the model.

An important metric to determine the efficiency of a model is the computational cost. Therefore, a simulation was performed using the finest mesh, i.e., 50x40x400 elements, to determine the total run time of each component of AniPFM when performing an FSI simulation. Due to the use of the IQN-ILS coupling scheme, the fluid and structural solver run in parallel i.e., both solvers compute a timestep at the same time, instead of sequentially. Due to the domain decomposition and the larger fluid mesh, the fluid solver took slightly longer than the structural solver for each iteration. Since they are run in parallel, only the run time of the fluid solver is of importance, and thus the computational resources of the structural solver are not included in the comparison. The resulting distribution of the computational costs is shown in Figure 25. As can be seen, the URANS calculations take almost 50% of the total run time, whereas the total AniPFM runtime is equal to 44.5% of the total run time. Furthermore, communication and mapping between the structural and fluid solver took roughly 5.7% of the runtime. Thus, the total runtime is roughly doubled by adding the AniPFM calculations when compared to a pure URANS simulation.

Additionally, the calibrated AniPFM shows the possibility of outperforming LES while requiring significantly lower computational resources. While further validation and testing are required, the results are very encouraging.

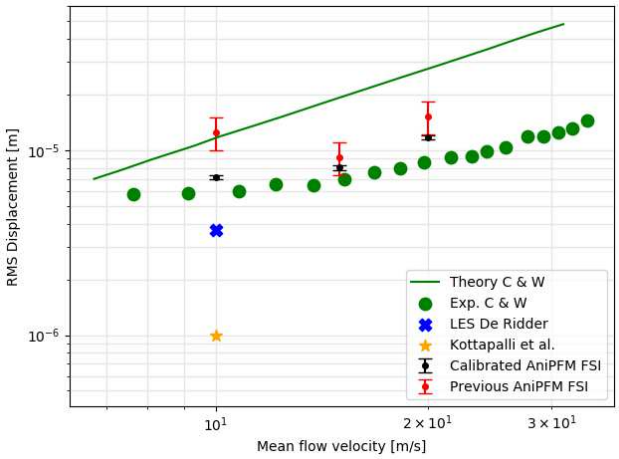

Figure 24: Comparison of the RMS vibration amplitudes of the calibrated AniPFM with the experimental results and other researchers' work.

For AniPFM to be computationally cheaper than an LES, the mesh must be at least twice as small, thereby neglecting the need for a smaller time step when using a finer mesh. For comparison, De Ridder (2015) performed an LES of the same geometry and inlet conditions, though for a reduced size rod. If the actual rod length was modelled, an equivalent mesh of 720 million cells would have been necessary. With the current AniPFM simulations, the cell count has been kept

below one million for even the finest simulations. Thus, the calibrated AniPFM shows the possibility of outperforming LES while requiring significantly lower computational resources. While further validation and testing are required, the results are very encouraging.

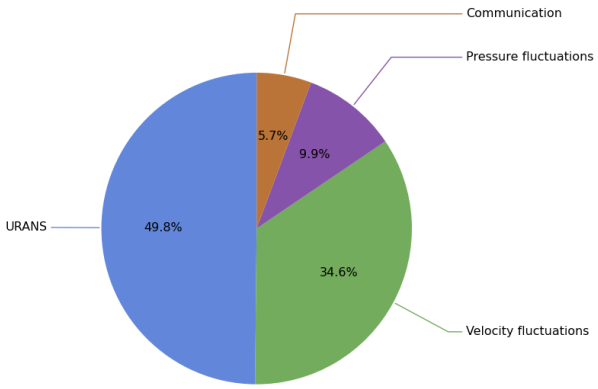

Figure 25:Computational costs of separate components of AniPFM for the brass beam case using the $50 \times 40 \times 300$ *mesh.*

6. CONCLUSIONS

In this paper, an optimized version of the anisotropic pressure fluctuation model is presented. AniPFM was developed to overcome found shortcomings in the original pressure fluctuation model, such as the lack of anisotropy in the Reynolds stress tensor and poor time correlation of the underlying Fourier modes. AniPFM is to be used in combination with a URANS simulation, coupled to a structural solver, in order to perform numerical simulations of turbulence-induced vibrations, such as for fuel rods in nuclear power plants. While the initial version of AniPFM gave promising and improved results, the effect of some of the model's parameters and modelling options on the results was not fully understood yet. Additionally, the values of these parameters stem from literature, in which they were tuned for other flow configurations, such as a 3D jet. As our intended application, being wall-bounded flow, is quite different, the sensitivity of the model on these parameters was investigated, in order to come to an optimized version of AniPFM. This was initially done on a pure flow case, viz. turbulent channel flow.

From this case, it was found that AniPFM gave better results when velocity fluctuations are generated using the Convection & Expenonetial Correlation time method than with the Pure Convection method. This is partly due to the former being more realistic, as it solves an actual advection equation instead of the modes simply being convected by the local mean flow. Moreover, the C&EC method gives results that are almost independent of the number of modes used and of the seed of the random number generator. Additionally, from the TCF case, it was also found that a modification factor $f_\tau = 25$ is preferred, and that the expression for the TKE peak length scale based on the local turbulent kinetic energy gives the best results. A final observation using TCF for sensitivity testing is that RMS pressure fluctuations at the wall can be reproduced quite accurately, using DNS data as reference, when the correlation factor is chosen correctly. This can be done for either of the two expressions for the cut-off length scale available in AniPFM.

Following the TCF sensitivity testing, AniPFM was used to simulate the brass beam experiment performed by Chen & Wambsganss (1972). This experiment was chosen because it closely resembles that of a nuclear fuel rod subjected to axial flow. Simulations confirmed, through polar plots of the displacement of the beam, that indeed the C&EC method gives better and more realistic results than the PC method. Additionally, using the settings optimized based on the TCF comparison study, the model also gives improved results for the beam's displacement when compared with previous versions of the model. Finally, overall, a good match with the experimental data is found, thereby demonstrating that the model was successfully optimized, at least based on this first comparison.

As a next step, AniPFM will be applied to other turbulence-induced vibration cases, to investigate if the optimized AniPFM also gives good results for other cases. Moreover, further development of the model is foreseen, such as the implementation of different energy spectra that can optionally be used for the individual velocity fluctuation component, such that anisotropy in the individual velocity fluctuation components can also be accounted for in the model.

ACKNOWLEDGEMENTS

The work described in this paper is part of the GO-VIKING project (Grant Agreement No. 101060826) funded by the Euratom research and training program 2022-2025 and that of the PIONEER research program at the Nuclear Research & consultancy Group, funded by the Ministry of Economic Affairs. The authors are grateful for their contributions. Also, the authors would like to thank the Delft University of Technology for supporting the research project and providing additional resources. Additionally, the research is partly supported by European Union's HORIZON MSCA Doctoral Networks programme, under Grant Agreement No. 101072344, project AQTIVATE (Advanced computing, QuanTum algorIthms and data-driVen Approaches for science, Technology and Engineering).

AVAILABILITY OF DATA

The data that support the findings of this study are available from the corresponding author upon reasonable request.

REFERENCES

Abe, H., Kawamura, H., and Matsuo, Y., 2001, "Direct numerical simulation of a fully developed turbulent channel flow with respect to the Reynolds number dependence", Journal of Fluids Engineering, 123 (2), pp. 382–393.

Abe, H., Matsuo, Y, and Kawamura, H., 2005, "A DNS study of Reynolds number dependence on pressure fluctuations in a turbulent channel flow", in: Proceeding of Fourth International Symposium on Turbulence and Shear Flow Phenomena, Begellhouse.

Adamian, D., and Travin, A., 2011, "An efficient generator of synthetic turbulence at RANS–LES interface in embedded LES of wall-bounded and free shear flows", in Computational Fluid Dynamics 2010, pp. 739–744. Springer Berlin Heidelberg.

Alzetta, G., 2018, "The deal.II library, version 9.0", Journal of Numerical Mathematics.

Antunes, J., Piteau, P., Delaune, X., and Borsoi, L., 2015, "A new method for the generation of representative time-domain turbulence excitations" Journal of Fluids and Structures, 58, pp. 1-19.

Auerswald, T., Probst, A., and Bange, J., 2016, "An anisotropic synthetic turbulence method for large eddy simulation. International Journal of Heat and Fluid Flow, 62, pp. 407–422.

Axisa, F., Antunes, J., and Villard, B., 1990, "Random excitation of heat exchanger tubes by cross-flows", Journal of Fluids and Structures, 4(3), pp. 321-341.

Bailly, C., and Juve, D., 1999, "A stochastic approach to compute subsonic noise using linearized Euler's equations", in 5th AIAA/CEAS Aeroacoustics Conference and Exhibit, Bellevue, WA, USA.

Basile, D., Fauré, J. and, Ohlmer, E., 1968, "Experimental study on the vibrations of various fuel rod models in parallel flow", Nuclear Engineering and Design 7 (6), pp. 517–534. doi:10.1016/0029-5493(68)90102-7.

Batten, P., Goldberg, U, and Chakravarthy, S., 2004, "Interfacing statistical turbulence closures with large-eddy simulation. AIAA Journal, 42(3), pp. 485–492.

Billson, M., Eriksson, L.-E., and Davidson, L., 2004, "Jet Noise modeling using synthetic anisotropic turbulence", in 10th AIAA/CEAS Aeroacoustics Conference, Manchester, UK.

Bos, N. van den, Zwijsen, K., Zuijlen, A.H. van, Frederix, E.M.A., and, Roelofs, F., 2022, "Turbulence-Induced Vibrations Prediction Through Use Of An Anisotropic Pressure Fluctuation Model", EPJ Nuclear Sciences & Technology.

Brungart, T. A., Lauchle, G. C., Deutsch, S., and Riggs, E. T., 1999, "Outer-flow effects on turbulent boundary layer wall pressure fluctuations", The Journal of the Acoustical Society of America 105 (4), pp. 2097–2106.

Bungartz, H.-J., Lindner, F., Gatzhammer, B., Mehl, M., Scheufele, K., Shukaev, A., and Uekermann, B., 2016, "preCICE – a fully parallel library for multi-physics surface coupling", Computers & Fluids, 141, pp. 250–258.

Castro, H.G., and Paz, R.R., 2013, "A time and space correlated turbulence synthesis method for large eddy simulations", Journal of Computational Physics, 235, pp. 742–763.

Chen, S.S., and Wambsganss. M.W., 1972, "Parallel-flow-induced vibration of fuel rods", Nuclear Engineering and Design, 18(2), pp. 253–278.

Davidson, L., and Billson, M., 2006, "Hybrid LES-RANS using synthesized turbulent fluctuations for forcing in the interface region. International Journal of Heat and Fluid Flow, 27 (6), pp. 1028–1042.

Degroote, J., Bathe, K., and Vierendeels. J., 2009, "Performance of a new partitioned procedure versus a monolithic procedure in fluid-structure interaction", Computers & Structures, 87 (11), pp. 793–801.

De Ridder, J.D., Degroote, J., Tichelen, K. van, Schuurmans, P. and Vierendeels, J., 2013, "Modal characteristics of a flexible cylinder in turbulent axial flow from numerical simulations", Journal of Fluids and Structures, 43, pp. 110–123. doi:10.1016/j.jfluidstructs.2013.09.001.

De Ridder, J.D., 2015, "Computational analysis of flow-induced vibrations in fuel rod bundles of next generation nuclear reactors", Ph.D. thesis, Ghent University.

DeSantis, D.D. and Shams, A., 2019, "An advanced numerical framework for the simulation of flow induced vibration for nuclear applications", Annals of Nuclear Energy, 130, pp. 218–231. doi:10.1016/j.anucene.2019.02.049.
Di Mare, L., Klein, M., Jones, W.P., and Janicka, J., 2006, "Synthetic turbulence inflow conditions for large-eddy simulation. Physics of Fluids, 18 (2).
El Bouzidi, S., and Hassan, M., 2015, "An investigation of time lag causing fluidelastic instability in tube arrays", Journal of Fluids and Structures, 57, pp. 264-276.
Elbanhawy, O., Hassan, M., and Mohany, A., 2020, "Simulation of motion-dependent fluid forces in fuel bundles", Nuclear Engineering and Design, 356, pp. 110373.
Elbanhawy, O., Hassan, M., and Mohany, A., 2021, "Modelling of fully-flexible fuel bundles", Nuclear Engineering and Design, 378, pp 111014.
EPRI, 2008, "Fuel Reliability Guidelines: PWR Grid-to-Rod Fretting", Technical report, 1015452. https://www.epri.com/research/products/1015452
Ewert, R., 2007, "RPM - the fast random particle-mesh method to realize unsteady turbulent sound sources and velocity fields for CAA applications", in 13th AIAA/CEAS Aeroacoustics Conference (28th AIAA Aeroacoustics Conference), American Institute of Aeronautics and Astronautics, Rome, Italy, May 2007.
Ewert, R., Dierke, J., Siebert, J., Neifeld, A., Appel, C., Siefert, M., and Kornow, O., 2011, CAA broadband noise prediction for aeroacoustic design. Journal of Sound and Vibration, 330 (17), pp. 4139–4160.
Fathali, M., Klein, M., Broeckhoven, T., Lacor, C., and Baelmans, M., 2008, "Generation of turbulent inflow and initial conditions based on multi-correlated random fields", international Journal for Numerical Methods in Fluids, 57 (1), pp. 93–117.
Goody, M., 2004, "Empirical spectral model of surface pressure fluctuations", AIAA Journal, 42 (9), pp. 1788–1794.
Hassan, M., Gerber, A., and Omar, H., 2010, "Numerical estimation of fluidelastic instability in tube arrays", Journal of Pressure Vessel Technology, 132(4), pp. 041307.
Hellsten, A., 2004, "New two-equation turbulence model for aerodynamics applications", PhD dissertation, Helsinki University of Technology.
Hirai, S., Fukushima, Y., Obayashi, S., Misaka, T., Sasaki, D., Ohmichi, Y., Kanamori, M., and Takahashi, T., 2019, "Influence of turbulence statistics on stochastic jet-noise prediction with synthetic eddy method", Journal of Aircraft, 56 (6), pp. 2342–2356.
Hu, Z.W., Morfey, C. L., and Sandham, N. D., 2006, "Wall pressure and shear stress spectra from direct simulations of channel flow", AIAA Journal, 44 (7), pp. 1541–1549.
Hu, N., Reiche, N., and Ewert, R., 2017, "Simulation of turbulent boundary layer wall pressure fluctuations via poisson equation and synthetic turbulence", Journal of Fluid Mechanics, 826, pp. 421–454.
Hu, N., Appel, C., Haxter, S., Callsen, S., and Klabes, A., 2019, "Simulation of wall pressure fluctuations on airbus-a320 fuselage in cruise flight condition", in 25th AIAA/CEAS Aeroacoustics Conference. American Institute of Aeronautics and Astronautics, Delft, The Netherlands, 2019.
Huang, S.H., Li, Q.S., and Wu, J.R., 2010, "A general inflow turbulence generator for large eddy simulation. Journal ofWind Engineering and Industrial Aerodynamics, 98 (10-11), pp. 600–617.
IAEA, 2019, "Review of Fuel Failures in Water Cooled Reactors (2006-2015)", IAEA No NFT-2.5, NE1864, Vienna, Austria.
IPCC (Intergovernmental Panel on Climate Change), 2023, "AR6 Synthesis Report: Climate Change 2023", Technical Report.
Jarrin, N., Benhamadouche, S., Laurence, D., and Prosser, R., 2006, "A synthetic-eddy-method for generating inflow conditions for large-eddy simulations", International Journal of Heat and Fluid Flow, 27 (4), pp. 585–593.
Kim, J., Moin, P., and Moser, R., 1987, "Turbulence statistics in fully developed channel flow at low Reynolds number", Journal of Fluid Mechanics 177, pp. 133–166.
Kim, Y, Castro, I.P., and Revell, A., 2013, "Divergence-free turbulence inflow conditions for large eddy simulations with incompressible flow solvers", Computers & Fluids, 84, pp. 56–68.
Kitagawa, T., and Nomura, T., 2003, "A wavelet-based method to generate artificial wind fluctuation data", Journal of Wind Engineering and Industrial Aerodynamics, 91 (7), pp. 943–964.
Klein, M., Sadiki, A., and Janicka, J., 2003, "A digital filter based generation of inflowdata for spatially developing direct numerical or large eddy simulations", Journal of Computational Physics, 186 (2), pp. 652–665.
Kleinhans, D., Friedrich, R., Schafferczyk, A.P., and Peinke, J., 2009, "Synthetic turbulence models for wind turbine applications", in Springer Proceedings in Physics, pp. 111–114. Springer Berlin Heidelberg.
Kottapalli, S., Sharma, S., Shams, A., Zuijlen, A.H. van, and Pourquie, M.J.B.M., 2017, "Numerical Simulation of Turbulence Induced Vibrations from URANS models using the Pressure Fluctuation Model.", NURETH-17, Xi'an, China.
Kottapalli, S., Shams, A., Zuijlen, A.H. van, and Pourquie, M.J.B.M., 2019, "Numerical investigation of an advanced U-RANS based pressure fluctuation model to simulate non-linear vibrations of nuclear fuel rods due to turbulent parallel-flow," Annals of Nuclear Energy, 128.
Kraichnan, R.H., 1970, "Diffusion by a random velocity field", Physics of Fluids, 13 (1).

Lamarsh, J.B., and Baratta, A.J., 2001, "Introduction to Nuclear Engineering", Prentice Hall, 3rd Edition
Laraufie, R., and Deck, S., 2013, "Assessment of reynolds stresses tensor reconstruction methods for synthetic turbulent inflow conditions. application to hybrid RANS/LES methods", International Journal of Heat and Fluid Flow, 42, pp. 68–78.
Lee, S., 2012, "Empirical wall-pressure spectral modeling for zero and adverse pressure gradient flows", AIAA Journal, 56 (5), pp. 1818–1829.
Lever, J. H., and Weaver, D. S., 1982, "A theoretical model for fluid-elastic instability in heat exchanger tube bundles.", Journal of Pressure Vessel Technology, 104(3), pp. 147-158.
Luk, K.H., 1993, "Pressurized-Water Reactor Internals Aging Degradation Study," Oak Ridge National Laboratory.
Nazari, T., Rabiee, A., and Kazeminejad, H., 2019, Two-way fluid-structure interaction simulation for steadystate vibration of a slender rod using URANS and LES turbulence models, Nuclear Engineering and Technology 51 (2), pp. 573–578.
Païdoussis, M.P, 1969, "An experimental study of vibration of flexible cylinders induced by nominally axial flow", Nuclear Science and Engineering 35 (1), pp. 127–138. doi:10.13182/nse69-a21121.
Price, S. J., and Païdoussis, M. P., 1986, "A single-flexible-cylinder analysis for the fluidelastic instability of an array of flexible cylinders in cross-flow", Journal of Fluids Engineering, 108(2), pp. 193-199.
Price, S. J., 1995, "A review of theoretical models for fluidelastic instability of cylinder arrays in cross-flow", Journal of Fluids and Structures, 9(5), pp. 463-518.
Rehman, S. A., El Bouzidi, S., Elbanhawy, O., Hassan, M., and Weaver, D., 2023, "Numerical Prediction of the Streamwise Fluidelastic Instability", Journal of Pressure Vessel Technology, 145(5), pp. 051402.
Rozenberg, Y., Robert, G., Moreau, S., 2012, "Wall-pressure spectral model including the adverse pressure gradient effects", AIAA Journal, 50 (10), pp. 2168–2179.
Saad, T., Cline, D., Stoll, R., and Sutherland, J.C., 2017, "Scalable tools for generating synthetic isotropic turbulence with arbitrary spectra", AIAA Journal, 55 (1), pp. 327–331.
Senthooran, S., Lee, D.-D., and Parameswaran, S., 2004, "A computational model to calculate the flow-induced pressure fluctuations on buildings", J. Wind Eng. Ind. Aerodyn. 92, pp. 1131-1145.
Sescu, A., and Hixon, R., 2012, "Generation of divergence-free synthetic turbulent velocity fields for LES/CAA applications", in 50th AIAA Aerospace Sciences Meeting, Nashville, Tennessee, USA, January 2012.
Shu, Y., Wu, J., Yang, Y., and Zhao, Z., 2019, "Fretting wear and fatigue life analysis of fuel bundles subjected to turbulent axial flow in CEFR", Science and Technology of Nuclear Installations 1–11. doi:10.1155/2019/5613737.
Shur, M.L., Spalart, P.R., Strelets, M.K., and Travin, AlK., 2014, "Synthetic turbulence generators for RANS-LES interfaces in zonal simulations of aerodynamic and aeroacoustic problems", Flow Turbul. Combust. 93, pp. 63-92.
Smirnov, A., Shi, S., and Celik, I., 2006, "Random flow generation technique for large eddy simulations and particle-dynamics modeling", Journal of Fluids Engineering, 123(2), pp. 359–371.
Wallace, J.M., Eckelmann, H., and Brodkey, R.S., 1972, "The wall region in turbulent shear flow", Journal of Fluid Mechanics 54 (1), pp. 39–48.
Wallace, J.M., 2016, "Quadrant analysis in turbulence research: History and evolution", Annual Review of Fluid Mechanics 48 (1).
Wallin, S., and Johansson, A.V., 2000, "An explicit algebraic Reynolds stress model for incompressible and compressible turbulent flows", Journal of Fluid Mechanics, 403, pp. 89-132.
Wambsganss, M., and Chen, S., 1971, "Tentative design guide for calculating the vibration response of flexible cylindrical elements in axial flow", Tech. Rep., doi:10.2172/4020578.
Weaver, D.S., Ziada, S., Au-Yang, M.K., Chen, S.S., Païdoussis, M.P. and Pettigrew, M.J., 2000, "Flow-induced vibrations in power and process plant components—progress and prospects", Journal of Pressure Vessel Technology 122 (3) (2000) 339–348. doi:10.1115/1.556190.
Wilcox, D.C., 1993, "Turbulence modelling for CFD", DCW Industries.
Xie, Z.-T., and Castro, I.P., 2008, "Efficient generation of inflow conditions for large eddy simulation of street-scale flows", Flow, Turbulence and Combustion, 81 (3), pp. 449–470.
Zwijsen, K., Bos, N. van den, Frederix, E.M.A., Roelofs, F. and Zuijlen, A. H. van, 2024, "Development of an Anisotropic Pressure Fluctuation Model for the Prediction of Turbulence-Induced Vibrations of Fuel Rods". Nuclear Engineering and Design, 425, pp. 113316